Multi-wavelength probe for tumor margin detection during breast conserving surgery

A proof of concept study

Rebecca Breda

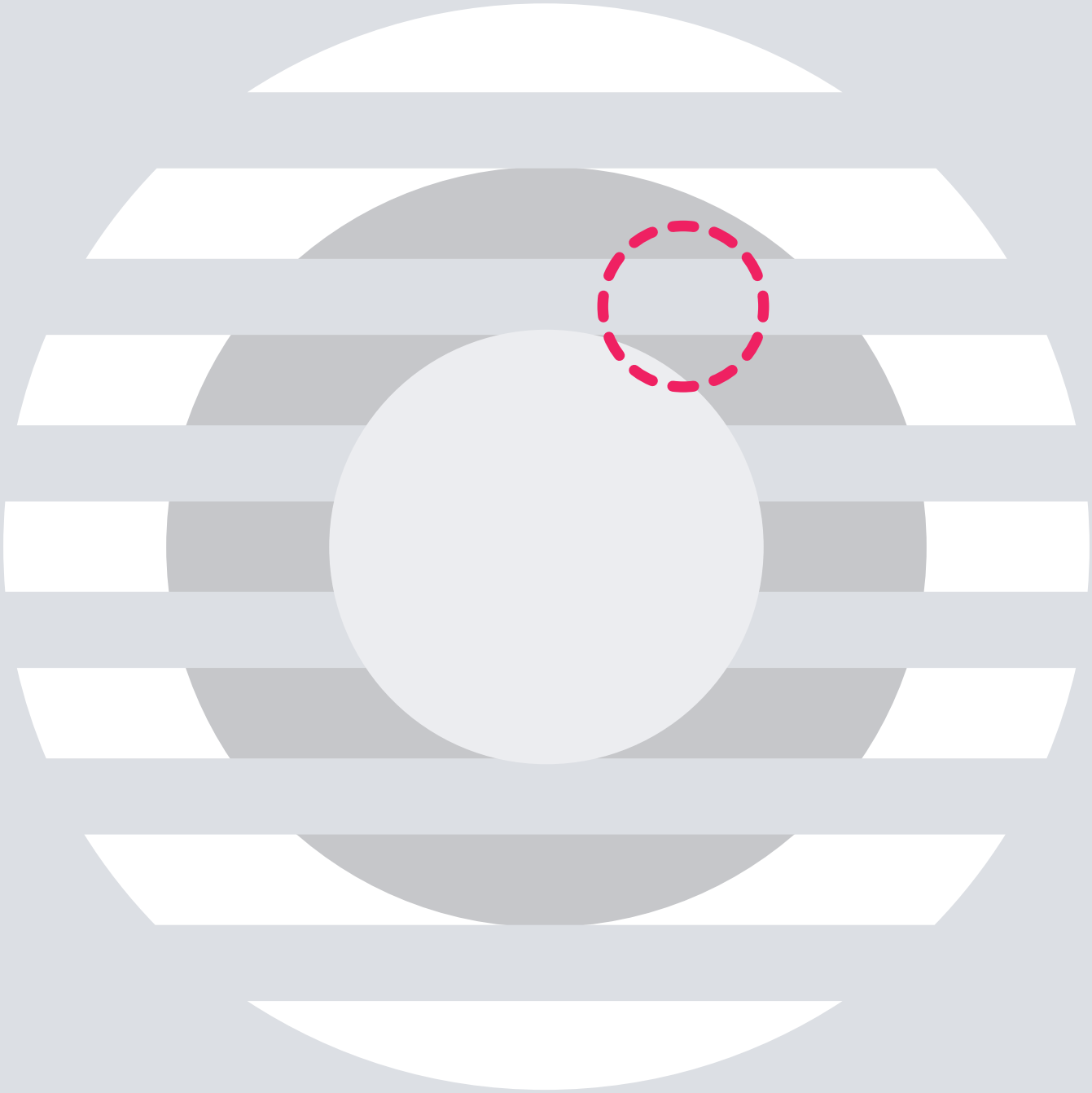

Master Thesis | MSc Biomedical Engineering

TU Delft

Multi-wavelength probe for tumor margin detection during breast conserving surgery

A proof of concept study

Author
Rebecca Breda

Master thesis
MSc. Biomedical Engineering
Faculty of Mechanical, Maritime and Materials Engineering (3mE)
Delft University of Technology

Graduation Committee
Chair | Prof. Dr. B.H.W. Hendriks
Faculty of Mechanical, Maritime and Materials Engineering (3mE)

Daily Supervisor | S. Azizian Amiri
Faculty of Mechanical, Maritime and Materials Engineering (3mE)

Committee Member | Prof. Dr. J. Dankelman
Faculty of Mechanical, Maritime and Materials Engineering (3mE)

External Committee Member | Dr.ir. S. Iskander-Rizk
Faculty of Mechanical, Maritime and Materials Engineering (3mE)

22 November, 2022

TU Delft PHILIPS

Acknowledgements

This report marks the final step of my thesis, and with it the end of the Biomedical Engineering MSc at the Delft University of Technology. It has been a long, incredibly interesting journey, that would not have been possible without the invaluable contribution of those around me. First of all, I would like to thank my committee members, for involving me in a project that I was so passionate about. I would like to express my gratitude towards my supervisors: Dr. Benno Hendriks, for sharing his knowledge and helping me see the bigger picture, and Dr. Jenny Dankelman, for her critical outlook and for guiding me through the graduation process. A special thanks goes to my daily supervisor, Sara Azizian Amiri, for trusting my judgment and helping me shape my own project. Her experience and continuous support were crucial to achieving these results. I am also grateful to Pascal Callaert for his collaboration and sharing the results of his research along the way. Throughout the project, I had to delve into fields that I had no experience in. The suggestions and aid from the technical staff of IWS, the Optics lab of 3mE, and ir. Frank Budzelaar, helped me move forward and overcome many obstacles. Lastly, I would like to express my deepest gratitude to all the people that have marked my experience in Delft. To my colleagues from BME, for the endless coffee breaks and moral support in these two years; to my friends and flatmates, for always being there to lighten up my day; and to Rob, for keeping me sane in these last months. I also want to thank Anna, Elena and my brother Klaus, for motivating me regardless of the distance. Finally, words are not enough to express my gratitude towards my parents, for making all of this happen.

Rebecca Breda
22 November, 2022

Abstract

Breast cancer is the most prevalent form of cancer among women, leading to 2.3 million new diagnosis and almost 685,000 deaths in 2020. Currently, one of the preferred treatments is breast conserving surgery (BCS), but its success depends on the correct identification of tumor margins during surgery. A promising optical intraoperative margin assessment technique is diffuse reflectance spectroscopy (DRS). However, the DRS instrumentation is complex, since it uses dedicated broad-range lights and sensors. In addition, the system is expensive and voluminous. Thus, a simpler alternative is desired. A possible approach is to probe the tissue's optical response at only a few relevant wavelengths.

This thesis, developed within an ongoing collaboration between TU Delft and Philips, represents a first proof-of-concept study towards the development of a multi-wavelength hand-held probe for real-time tumor detection during BCS.

A multi-wavelength sensor was developed for testing based on an existing prototype, able to measure with an infrared photodetector the optical response from two independent light emitting diodes.

The working principle of the detection system was based on the known differences in fat/water-ratio between healthy and tumor tissue. It was investigated whether the optical response of tissue phantoms with different fat and water content, measured with infrared LEDs in a transmittance-based configuration, could provide a means to quantify the composition of the phantoms. A measurement method was proposed based on the linear relationship observed between the percentage of fat in the phantoms and the ratio of transmitted light intensity measured at 970 nm or 1300 nm, and 1200 nm. The test was repeated with new phantoms, and it was found that the parameters of the fat-intensity relationship varied between the experiments. The scattering parameter was identified as the main cause of this variation.

To demonstrate the feasibility of integrating the system in a hand-held device, the sensor was tested with optical fibers in a reflectance-based configuration. Infrared lasers were found to be suitable light sources to detect differences in reflected light intensity depending on the probing wavelength and phantom composition. However, the wavelengths of the available lasers were not significant for tissue discrimination, so the working principle of the measurement system was not tested in this configuration.

Overall, the results demonstrated that it is possible to use multi-wavelength optical measurements to detect differences between healthy and tumor tissue based on the fat and water concentrations. Further investigation is required to determine a robust method which allows to exactly quantify the tissue content based on the measured reflected intensity. Furthermore, following miniaturization and optimization, the sensor is suitable for integration in a hand-held surgical instrument. Despite the limitations, this study reveals the potential of multi-wavelength optical devices for tumor detection in breast, and encourages further research for their integration in the surgical practice.

Contents

Table of Contents

List of Figures

List of Tables

Abbreviations

Abbreviation	Definition
ADC	Analog to digital converter
BCS	Breast conserving surgery
DRS	Diffuse reflectance spectroscopy
f/w-ratio	fat/water ratio
IMA	Intraoperative margin assessment
IR	Infrared
LED	Light emitting diode
MPE	Maximum permissible exposure
NIR	Near-Infrared
NOHD	Nominal ocular hazard distance
PWM	Pulse-width modulation
SB	Sodium Benzoate
SD	Standard deviation
SDS	Source-detector Separation
SNR	Signal-to-noise Ratio
TG	Transglutaminase
TIA	Transimpedance amplifier

1.
Introduction

In 2020, 2.3 million women were diagnosed with breast cancer worldwide [1]. Likewise, approximately 15.000 new cases and 3.200 deaths were recorded only in the Netherlands in the same year [2, 3]. To face this problem, effective treatment methods are becoming increasingly necessary to improve the survival rate of cancer patients.

Today, the majority of early-stage invasive tumors are removed via breast conserving surgery (BCS) [1, 4], a minimally invasive technique that aims to resect only the primary tumor, along with a small margin of healthy tissue surrounding it (called “negative margin”) [4, 5]. Correct identification of the tumor margins is crucial to guarantee the success of BCS, as an incomplete resection of all cancer cells can lead to recurrence [6, 7]. On the contrary, excessive resection causes inferior cosmetic outcomes and longer recovery times [8]. Currently, the resection margins are identified preoperatively using imaging techniques. After the surgery, histopathological analysis is performed on the excised lump [9]. If tumor cells are found on the outer edge of the removed lump, the margin is defined as ”positive”, indicating that some malignant tissue is still in the body. As the analysis of the sample is only done after the primary surgery, if a positive margin is found, a second surgery is often required to remove the leftover tumor [8, 9]. Being able to correctly identify the tumor margins in real-time would reduce the chances of re-excision, and improve the success rate. For this purpose, multiple intraoperative margin assessment (IMA) techniques have been developed in recent years. However, they are often not practical, and a second incision is still necessary in 20-30% of cases [5, 6, 9].

Recent studies demonstrated the possibility to use diffuse reflectance spectroscopy (DRS) as an IMA technique for breast cancer identification [10–13]. DRS is an optical technique that uses a light source in a broad wavelength range to probe tissue and exploits the optical response to estimate the tissue composition. It is non-invasive, can be used in real time and does not affect tissue properties or composition, so it can be combined with other imaging techniques. Its working principles and instrumentation are described in more detail in Appendix A. In recent years, TU Delft and Philips joined efforts to investigate the integration of DRS into an electrosurgical knife to be used during BCS. Despite being a promising technology, DRS turns out to be bulky and expensive, so a simpler alternative is sought for integration into surgical instruments. Researchers have proposed to simplify DRS by inspecting only a few relevant wavelengths instead of the full spectrum [14–16], but this concept has not been extensively tested in practice.

Based on this idea, the DRS console could be replaced by a new, simpler device that uses a number of photodetectors and single-wavelength light sources. This simplification would decrease the complexity of the machine and the size of its components, resulting in a small system that could be integrated in a hand-held probe or in a electrosurgical knife without the need for external cables, computers or voluminous machines — not suitable for the operation room.

To develop such a technology, the first step is to prove its feasibility by answering the following research question:

Can we use multi-wavelength optical measurements for real-time discrimination of tumor tissue during BCS?

In the context of the collaboration between TU Delft and Philips, a multi-wavelength sensor prototype was already designed by S. Azizian Amiri, but never tested. This thesis aims at providing a proof of principle of the concept expressed in the research question, by using the existing device to demonstrate that small multi-wavelength systems are a promising tool towards intraoperative tissue discrimination in breast.

This report presents the process and results of the work conducted during the thesis project. Ch. 2, introduces the research methodology: Section 2.1 explains the chosen research approach based on the findings of the literature review; Section 2.2 presents the research sub-questions derived from the main research objective, and the resulting report structure. After this, the design and operation of the sensor board developed by S. Azizian Amiri are described in Ch. 3. To implement a multi-wavelength optical system for IMA, two aspects needed to be investigated: firstly, the working principle of the sensor (the mechanism that allows us to discriminate different tissues) was explored in Ch. 4 and 5; secondly, in Ch. 6, the sensor was evaluated from a physical perspective to determine whether it could be used for real-time measurements in a surgical setting. In Ch. 7, an overall discussion of the results is laid out, and consequently future perspectives and recommendations are proposed. Finally, Ch. 8 summarizes the findings and links the project outcome to the initial research question.

2.

Research Approach

2.1. Background & Research Approach

This thesis was approached with the ultimate long-term goal of developing a hand-held probe for real-time tumor margin detection in breast. The overcomplicated mechanisms of DRS ignited this research question. So far, the above mentioned collaboration between TUDelft and Philips led to the exploration of DRS integration in hand-held needles or electrosurgical knives [12, 17–19]. Specifically, the intended use of the smart electrosurgical knife and its requirements for surgical implementation were explored in a concurrent graduation project by P. Callaert.

From the literature review conducted prior to this thesis, and the analysis of the current design of the mentioned DRS instruments, it was found that the integration of DRS into surgical devices demands a set of requirements:

- **In-vivo tissue inspection**. To measure tissue in-vivo with a hand-held device, the light sensor and detector need to be beside each other (reflectance-based configuration), rather than on opposite sides of the probed tissue (transmittance-based configuration).
- **Tumor detection with a margin of healthy tissue of at least 2 mm**. The amount of healthy tissue around the tumor after resection is determined by the probing depth of the device, which must be 2mm. This can be obtained by setting the distance between the sensor and the detector at around 1-4 mm, depending on the light source choice and setup [17, 18]. To achieve such precision, optical fibers are employed to transport light from and to the tip of the instrument.
- **Real-time information on the tissue type**. Based on a single optical measurement of the tissue, or average of multiple measurements, it should be possible to extract a parameter that represents the tissue properties. The interpretation of the parameter should then allow to directly determine if the probed tissue is malignant or benign in real-time.

Taking these requirements into account, in order to simplify DRS, it is necessary to understand how the technology works for tumor detection. Relevant studies showed that:

- **An effective discriminating factor between tumor and healthy tissue is the ratio between fat and water content (f/w-ratio)**. Different classification algorithms have been proposed (and in certain cases tested) based on the estimation of the water and lipid content [10, 12, 16, 20].
- **Although DRS inspects a broad light range, information regarding specific tissue properties is carried by different wavelengths**. Thus, depending on the application, a subset of relevant wavelengths can be used to probe the tissue without losing the optical information that enables tissue discrimination in DRS.

The thesis' research question entails a multitude of aspects, related both to the optical properties of the tissue and the interpretation of the optical signal, and to the physical requirements of the device and its ability to measure under specific conditions. Investigating all of them simultaneously would require complex and highly specific setups. At the same time, it would limit the application of the results to the intended use, not leaving space for generalization to other similar contexts. As a result of these considerations, a broader research approach was adopted. The main research question was divided into two independent research lines:

1. **Working principle:**
   The aim of the first research line was to define the mechanism that allows the multi-wavelength sensor to discriminate between benign and malignant breast tissue. This could consist of a mathematical formula, model or calibration curve that correlates the tissue properties with the quantity measured by the sensor - i.e., the intensity of light sources in different wavelengths after interaction with tissue.

2. **Instrumentation:**
   The second research line aimed to demonstrate the feasibility of using the device in a reflectance-based configuration with optical fibers. Hence, addressing the first two aforementioned requirements, necessary for the integration of the system in a hand-held probe for in-vivo measurements.

2.2. Research Sub-questions & Report Structure

The sensor board developed by S. Azizian Amiri was the vehicle that facilitated the experimentation throughout the development of this project, which consisted of two different phases. The first phase focused on testing and optimizing the electronic design to obtain a working device; these results are reported in Ch. 3. The second phase embodied the investigation of the two research lines, through a series of experiments described hereafter.

Working principle

To develop the working principle of the optical discrimination device, a range of infrared LEDs were used with the sensor board in a transmittance-based configuration. Based on the differences in fat/water-ratio between healthy and tumor tissue, the goal of the research was reframed to develop a device that could accurately measure fat and water concentrations. As a consequence, a first experiment was designed to gather data and propose a proof-of-concept of the working principle. The following research sub-questions guided the study:

1. **Are there differences in the detected signal at different wavelengths for varying fat and water concentrations?**
2. **Which wavelengths are relevant?**
3. **What formula can we use to estimate the fat and water content from these measurements?**

The motivations, the methods, and the results of the aforementioned experiment are described in Ch. 4.

Following this first test, Ch. 5 covers the development of a second experiment performed to validate the results of the former. To do so, this experiment was shaped by the following research sub-questions:

1. **Are the results of the first test repeatable?**
2. **Is the relationship between fat content and measured intensity consistent with the first test?**
3. **Is the fat-intensity relationship robust against scattering?**

Instrumentation

The second research line was investigated in Ch. 6 to determine whether the multi-wavelength system could be suitable for integration in a hand-held probe. The sensor board was used with fiber-coupled lasers and a fiber-coupled photodiode, mounted aside each other for reflectance-based measurements. Multiple small tests were executed to determine the performance of the sensor in this configuration, guided by two research sub-questions:

1. **Is the optical signal detectable in reflectance-based measurements?**
2. **Can differences in fat concentrations be distinguished in the detected signal?**

In this chapter, the objectives and the research sub-questions of each experiment were presented together to provide an overview of the whole project. Fig. 2.1 gives an overview of the thesis structure, highlighting the bifocal essence of the adopted approach, along with its implications for the structure of the report. In addition, the objectives and research sub-questions of each experiment are introduced again at the beginning of the respective chapters.

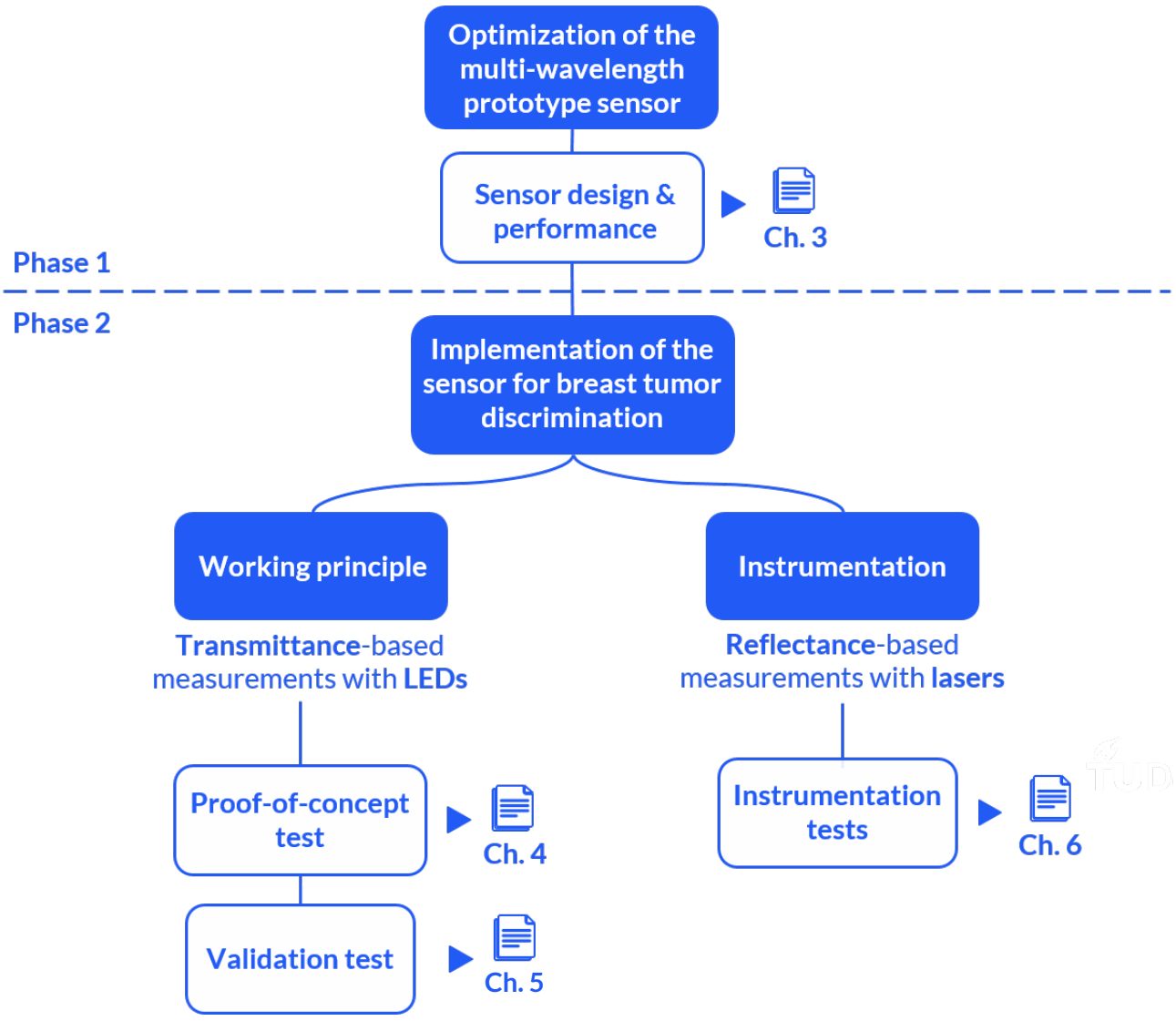

Figure 2.1: Schematic representation of the research approach adopted during the thesis project, and its impact on the structure of the report.

3.

Sensor Design & Performance

3. Sensor Design & Performance

As previously mentioned, a prototype multi-wavelength sensor was designed by S. Azizian Amiri and fabricated at Philips. The prototype was designed to simultaneously control multiple light sources and detect a readable optical signal for testing with tissues and phantoms. The first phase of the project consisted of testing the prototype for the first time, and evaluating the potential use of it for further studies to obtain a working device that could be easily adaptable to different test setups. The main challenge was achieving a sufficient sensitivity and signal-to-noise ratio (SNR).

In this context, the board was programmed to ensure its correct operation. This process was carried out iteratively by analyzing its performance, which led to small modifications of the circuit design. Hereafter, this chapter presents an explanation of the final circuit and the various aspects of the device's operation. Further optimization of the sensor's performance in terms of accuracy, precision and ease of use are suggested in Ch. 7 as future recommendations.

3.1. Circuit

The prototype board is divided into two main functional modules: the light source driver and the signal acquisition module, controlled by a Teensy 3.6 microcontroller (PJRC, USA) - the

”brain” of the circuit - programmed via the open-source Arduino software (Arduino IDE 1.8.19, Arduino, Italy). The light source driver module is used to independently control and power two light sources such as LEDs or laser diodes. The signal acquisition module is responsible for the timing and control of a photodetector and for the processing of the sensor signal, which can be recorded and transmitted to a computer via the microcontroller. Fig. 3.1 depicts the general block diagram of the device, while Fig. 3.2 shows a picture of the prototype. A more detailed explanation of the electronic design and operation of the prototype is described in the following sections.

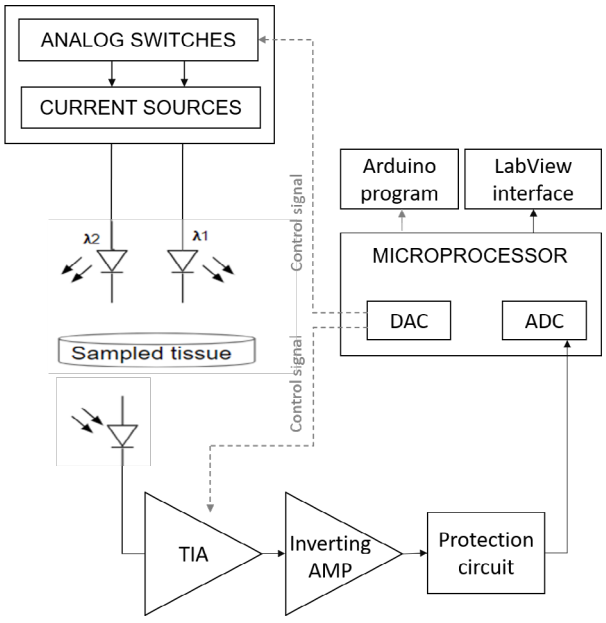

Figure 3.1: Block diagram of the device, including the light source driver block, the signal acquisition block and the microprocessor.

3.1.1. Light Source Driver Module

The light source driver module consists of two independent voltage-controlled current sources, which output two different constant current levels that power the light sources. The circuit schematic of one of the current sources is shown in Fig. 3.3. For each of these sources, the 5 V output voltage from the Teensy is converted into the desired

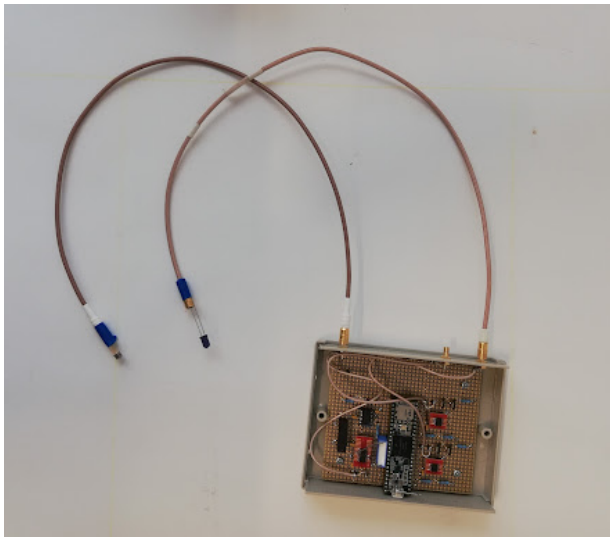

Figure 3.2: Picture of the electronic board, with one LED and sensor connected via coaxial cables.

current level via a general-purpose operational amplifier (TLV2372, Texas Instruments, USA) and an N-channel enhancement mosfet (NDT451AN, Onsemi, USA). Then, the signal is transmitted to the light source through a coaxial cable. The input voltage of the amplifier is selected by means of a voltage divider (*R1, R2*), while the current level is set by a source resistor, *Rsource*. To comply with the specifications of different LEDs and lasers, the value of *Rsource* was chosen based on simulations in the dedicated software Micro-Cap (Spectrum Software, USA) to obtain current sources around 46 mA and 100 mA. A second mosfet in series with *Rsource* acts as a light switch, which is controlled via software through a Teensy digital output pin. The circuit used for the simulation is reported in Appendix B.

3.1.2. Signal Acquisition Module

The signal acquisition module mainly comprises an infrared InGaAs photodiode (FGA01, Thorlabs, USA), connected to the board via a coaxial cable, and a precision switch integrator transimpedance amplifier (IVC102, Burr-Brown, USA). The photodiode outputs a current proportional to the amount of detected light, which is converted into voltage and amplified by the transimpedance amplifier (TIA). The (negative) signal from the TIA is then inverted by a unity-gain inverting amplifier (TL071CP, Texas Instruments, USA) to obtain a positive signal, readable by the Teensy. After a voltage limiting step that serves as input pin protection, the signal is converted into a digital signal via the Teensy integrated ADC. To power the TIA, A DC/DC converter is used to step-up the

input voltage of the Teensy and obtain a 15 V power line. The complete circuit schematics are depicted in Fig. 3.4. As the TIA dictates the operation and acquisition sequence of the signal, it is described in more detail in the following paragraphs.

Contrary to traditional transimpedance amplifiers, the TIA used in this project, described in Fig. 3.5, integrates low-level input currents for a user-determined period *Tint*, storing the resulting output voltage in the internal capacitor *Cint*. The integrating behavior reduces noise by averaging the input noise of the sensor, amplifier and external sources. Simultaneously, *Tint* allows for very high gain levels, which can be easily changed via software according to the application.

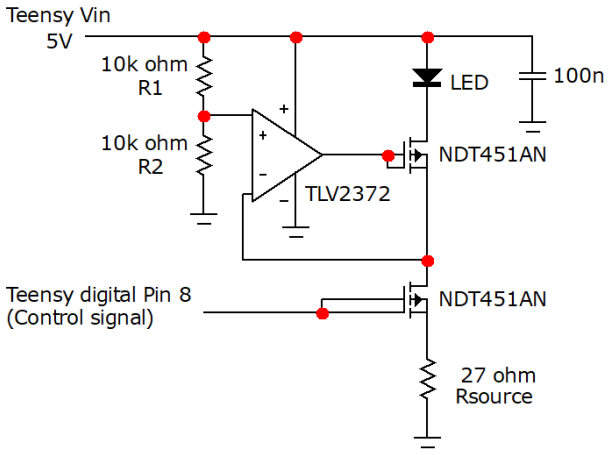

Figure 3.3: Circuit schematics of the voltage-controlled 46 mA current source. The 100 mA current source presents a similar circuit, connected to the Teensy digital pin 9, with a R_{source} value of 12 ohms.

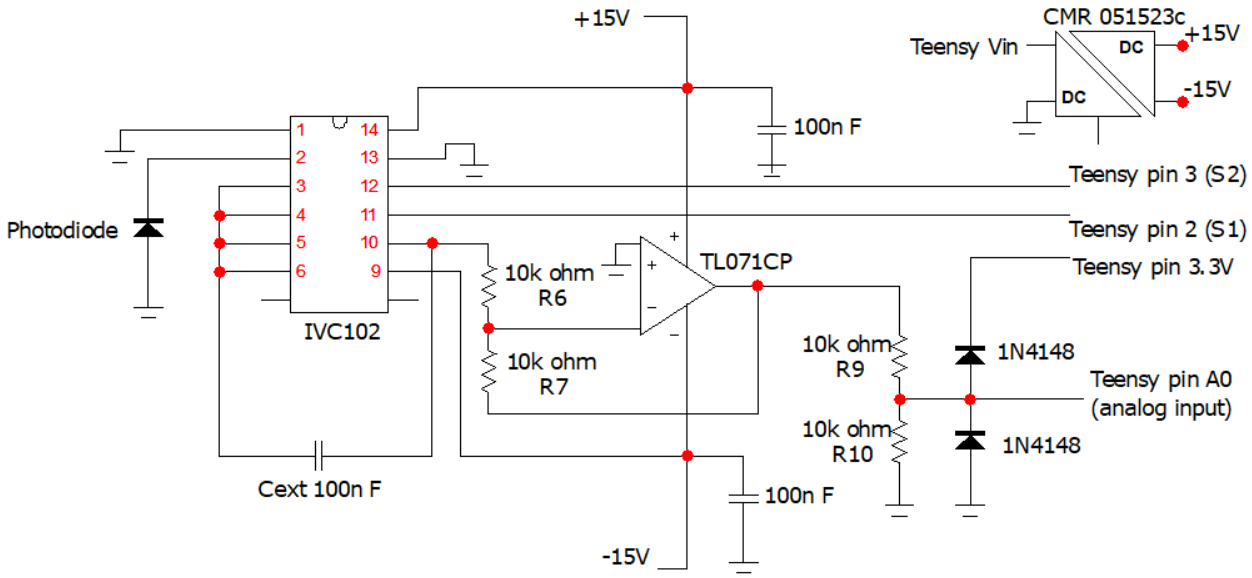

Figure 3.4: Circuit schematic of the signal acquisition module.

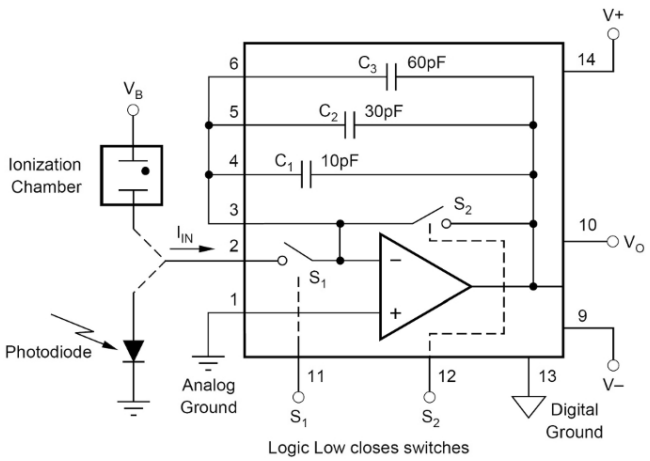

Figure 3.5: Circuit schematic of the IVC102 component by Burr-Brown, taken from the specification sheet. The ionization chamber in the figure is not present in reality.

The operation of the TIA works as follows: the measurement cycle is divided into four phases, determined by the opening and closing of two switches (*S1, S2*). *S1* and *S2* are controlled by two independent digital signals from the Teensy. First, a *reset* phase is necessary to reset the integrator to a 0 V level. Then, a *pre-integration hold* period allows to completely change the state of the switches. This is followed by the *integration period*, in which the sensor is connected to the amplifier and the signal is integrated. Afterwards, during the *post-integration hold* period, a stable output voltage that represents the effective output can be measured. The operation of the circuit is illustrated in 3.6.

The gain and reset time of the amplifier are determined by the internal capacitance of the IVC102. An external capacitor of 100 nF is connected to the ones already present, obtaining a total *Cint* of 100.1 nF. Higher *Cint* limits the slew rate and increases the maximum achievable *Tint*, which can be beneficial for noise reduction and compensation of timing inaccuracies at the software level. On the other hand, high *Cint* decreases the effective transimpedance gain according to the formula $Vo = -Iin * Tint/Cint$ (for a constant input current *Iin* after the integration period). Furthermore, it requires slightly larger reset times in the range of tens of microseconds. For testing purposes, high *Cint* and *Tint* were preferred to increase signal quality at the cost of measurement speed, which was considered secondary.

3.2. Operation

3.2.1. Measurement Cycle

The measurement cycle of the sensor is dictated by the operation of the TIA. Since the sensor is only active during the integration period, the light sources are only turned on for the duration of *Tint*. The effective sensor output is then recorded during the hold period via the Teensy ADC. The signal is sampled at the native Teensy sampling frequency and stored for further processing. A resolution of 13 bits is employed with the 1.2 V internal reference of the Teensy, which provides a more stable reference than the standard 3.3 V output. Thus, the detected signal is in the ADC range of 0-8191, corresponding to 0-1.2 V. Fig. 3.7 shows the digital control signals and measured output at the different stages of the measurement cycle, which correspond to the phases of the IVC102 operation, explained previously.

To compensate for the TIA offset, a two-point difference measurement is taken between the pre- & post-integration hold during each measurement cycle. The values sampled during each hold period are then averaged and subtracted from each other. As a result, a single voltage value is obtained at the end of each measurement cycle. The latter is then transmitted to the computer via serial communication, where the measured signal can be plotted real-time and recorded in a file via a LabView interface (LabView, National Instruments, USA).

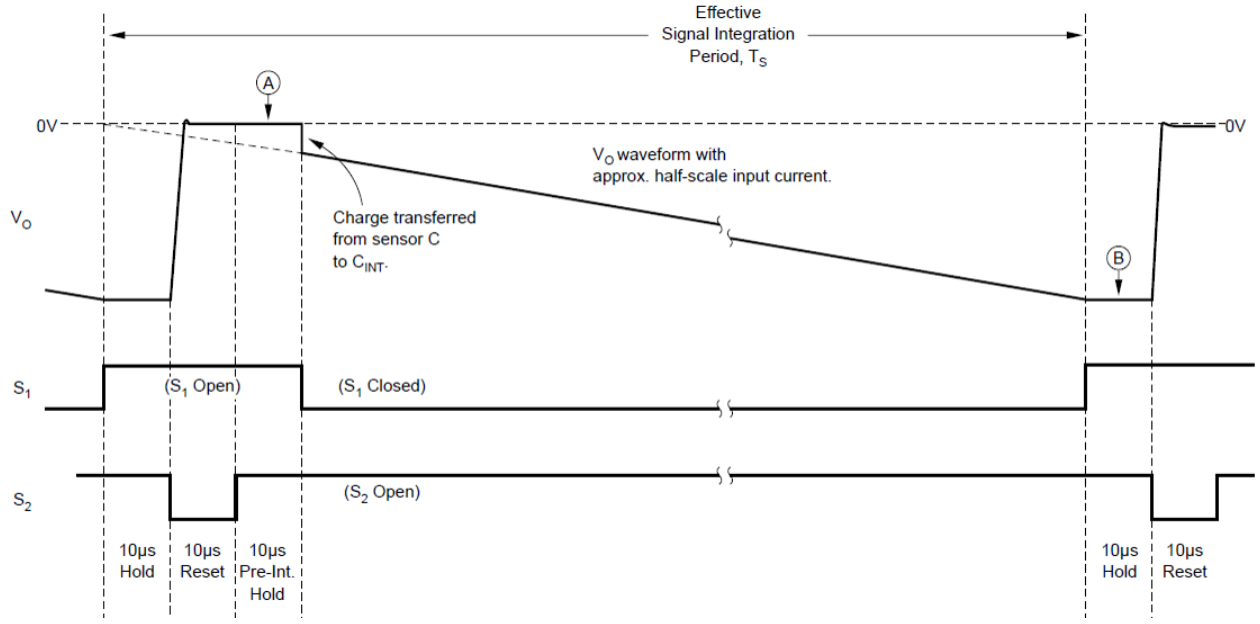

Figure 3.6: Operation cycle of the IVC102 transimpedance amplifier (Burr-Brown). Taken from the data sheet of the component provided by the manufacturer.

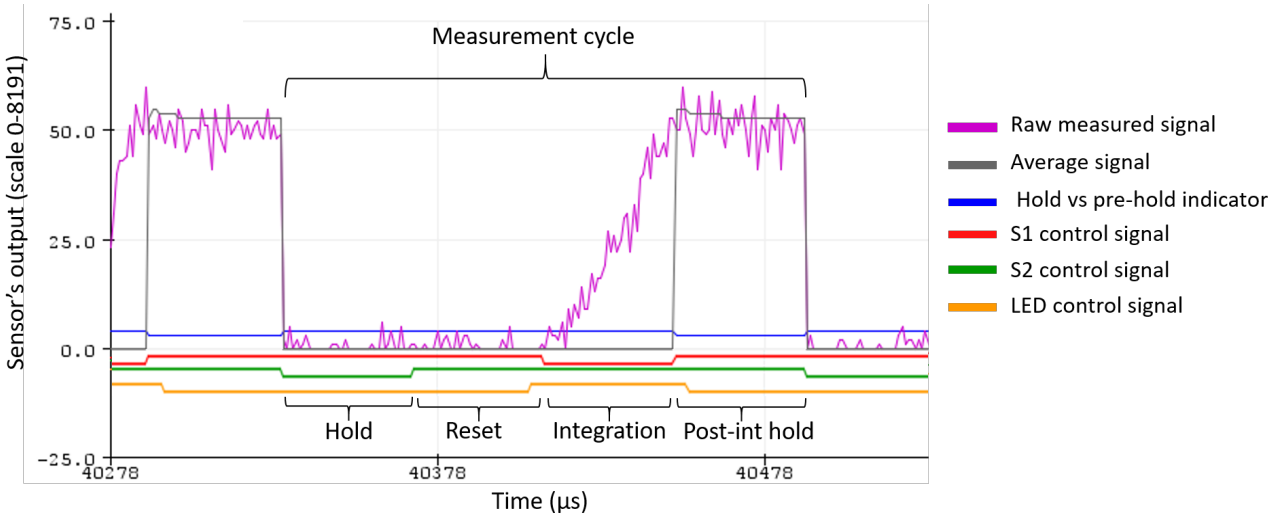

Figure 3.7: Screenshot of the Arduino serial plotter, to illustrate the programmed measurement cycle. The graph shows the output before averaging, along with the control signal for the different switches. The serial port of the Arduino software runs at a lower frequency than Teensy, so the illustrated signal contains fewer samples than the actual measured signals.

3.2.2. Light Source Timing

When multiple light sources are employed simultaneously, the measurement cycle remains the same, but the lights are turned on alternatively. The measured output is only recorded at the end of two full cycles, so that two voltage values, corresponding to the two sources, are acquired. Timing of the light sources is particularly important for signal quality and durability of the components. LEDs and laser diodes are prone to heating, which can result in a drift in the emitted power and wavelength. To enable passive cooling, the duty cycle of the diodes needs to be carefully considered. One approach is to increase the duration of the hold and reset periods, increasing the off-time of the light sources, at the expense of lower overall sampling frequency. Another approach is to use pulse-width modulation (PWM) with a low duty cycle. Although this method can achieve stable signals and increase the lifetime of the diodes, it can be a source of noise and decrease the effective source current, leading to lower power outputs. The optimal method, or combination of both, depends on the specific conditions under which the device is used.

3.2.3. Calibration and ambient light compensation

Calibration

Different LEDs and laser diodes have different power outputs, depending on the corresponding specifications and the selected driving current. Moreover, the responsivity of the sensor (in the 800-1700 nm range) is wavelength-dependent. To evaluate tissue responses with different LEDs, a calibration process is carried out taking a reference signal for each wavelength, which is then used to normalize the corresponding data.

Ambient Light Compensation

Another possible issue with the described setup is interference from external light, which might lead to artifacts in the signal. For this purpose, a background measurement can be performed by measuring the sensor's response when the source diodes are off and subtracting the detected value from all the measurements.

Real-time Feedback

For the purpose of testing, most of the signal processing was not implemented within the Arduino script, as the unprocessed signals were useful for the interpretation of the results. Features such as automatic ambient light removal can be easily implemented in future iterations, as well as a separate reference acquisition sequence. The purpose of this project was to investigate the relationship between the measured intensity and the chromophore content. Once this relationship is well-defined via a function or look-up-table, real-time conversion of the measured data into the desired parameters can be implemented in the source code to provide real-time feedback.

3.3. Preliminary Analysis

3.3.1. Setup Choice

Working Principle Tests

To determine the working principle of the discrimination device, the tissue response at many wavelengths needed to be investigated. Thus, low cost and high availability were chosen as criteria to determine the light sources used in the first experiment; as a consequence, LEDs were chosen.

Based on the requirements for surgical implementation, defined in Ch. 2, the use of optical fibers was suggested for light transport. However, the availability of off-the-shelf fiber-coupled LEDs is limited, and custom-made products increase cost and production times. For the purpose of testing the working principle of the device, it was thus decided to perform the first tests with bare LEDs.

Many examples in literature show the use of LEDs in reflectance mode (light source and sensor placed next to each other, on the same side of the probed tissue) [21–25]. However, due to the relatively low power output of most LEDs, preliminary tests did not achieve a detectable reflectance signal in this configuration. Transmittance measurements (LED and sensor facing each other), on the other hand, cause less light loss within the tissue. Although this configuration is different from what is used in DRS, it still allowed us to investigate the effect of the probing wavelength and tissue content on the detected optical signal.

Instrumentations Tests

For the second research line, a reflectance-based configuration and the use of optical fibers were important requirements. Preliminary tests showed that the power output of LEDs was too low to detect a signal in this configuration. Conversely, laser diodes can usually achieve a higher power output and thus less light loss in tissue, thanks to their non-collimated beam. Furthermore, lasers are more precisely focused at a specific wavelength compared to LEDs. Off-the-shelf fiber-coupled lasers are available in different wavelengths and can be easily mounted in a reflectance-based configuration. Thus, lasers were chosen as the optimal light source for this experiment.

3.3.2. Signal Characterization

After obtaining a working prototype, preliminary tests with LEDs were performed to characterize the measured signal. Fig. 3.8 displays the raw signal before averaging, acquired during a single hold period with a duration of 100 ms. For the measurement, the integration time was set at 200 ms, resulting in a sampling frequency of 1 kHz. The signal was recorded and plotted in Matlab (MathWorks, USA) along with a Q-Q plot to evaluate the distribution of the noise. During the hold period the photodetector is disconnected from the TIA, meaning that any variation in the signal is purely due to electrical noise or interference. The Q-Q plot was relatively linear, suggesting a normal distribution of noise. The hypothesis was corroborated with a chi-square test (p-value 0.61). According to this finding, the signal can be averaged during each hold period without losing information.

The test was repeated to evaluate the noise levels at different voltage values. The overall SNR of the raw signal was satisfactory for voltage values above 30 mV, ranging from 20 dB onwards. For small voltage levels, the SNR of the raw signal was relatively low, falling below 20 dB. Nonetheless, once the averaging was performed the recorded values were very stable. This demonstrated that the sensor's output was consistent and robust against external interference, instability of the LEDs or other sources of noise.

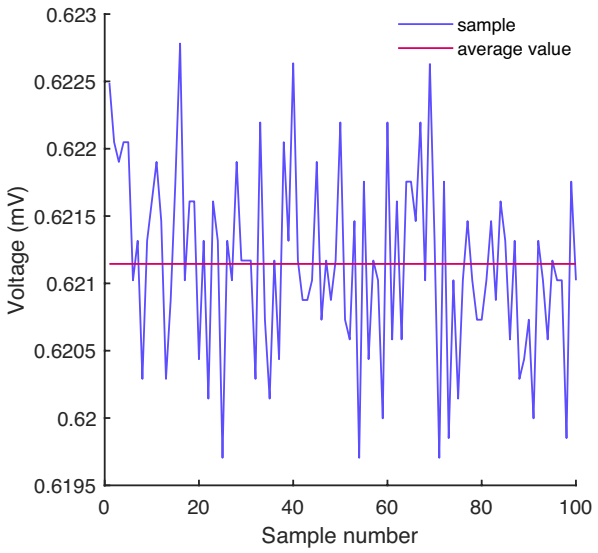

a) Sample Intensities

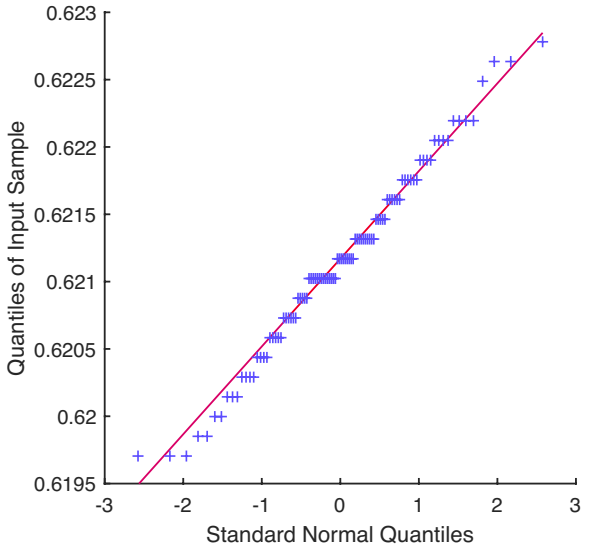

b) Q-Q Plot of Sample Intensities

Figure 3.8: a) shows the raw signal, acquired by the Teensy during a single post-integration hold period of 100 ms, before and after averaging. b) represents the Q-Q plot of the sample data, to evaluate the distribution of the noise. The linear trend of the points demonstrates that the noise has an approximately normal distribution.

4.

Proof of Concept Test

4. Proof-of-Concept Test

The response of tissue to light at different wavelengths depends on its morphology, structure and composition, which determine the intrinsic scattering and absorption properties of the specific tissue type. As a result of the literature review's findings, previously discussed in Ch. 2, it was decided to use the optical parameter associated with the absorption of fat and water, the f/w-ratio, as the discriminative parameter between healthy and tumor tissue in breasts. Thus, instead on focusing directly on the discrimination between tissue types, the sensor only needs to accurately measure fat and water concentrations. These quantities can then be converted into information concerning the tissue type based on existing classification algorithms [10, 12, 14, 26]. To reach this goal, three research questions were formulated in Section 2.2:

1. Are there differences in the detected signal at different wavelengths for varying fat and water concentrations?

2. Which wavelengths are relevant?

3. How can we estimate the fat and water content from these measurements?

A first test was carried out to investigate the research questions. Tissue-mimicking materials (phantoms) with different lipid and water concentrations were used to study whether differences between measured light intensity values after interaction with tissue could be detected. The sensor board was used to control a range of LEDs, to study the influence of the probing wavelength on the optical response of the phantoms. Full spectrum DRS measurements of the same phantoms were used for validation of the results.

In this chapter, the principles behind the selection of specific wavelengths are explained. Then, the experimental set-up and methods for both the LED and DRS test are presented, along with the results of the tests. Comparison of the results with the full spectral response and a-priori knowledge is then carried out to find a function or look-up-table able to describe the relationship between measured values and f/w-ratio. Finally, the results of the analysis are evaluated and compared with existing literature, to identify the limitations and relevant findings of the study.

4.2. Mini-review for wavelength selection

Accurate wavelength selection is of utmost importance to increase the chances of success of this novel multi-wavelength detection method. Existing literature was consulted to guide this choice, and the findings are reported hereafter.

The most relevant features in the reflectance spectrum associated with the f/w-ratio are in correspondence to the absorption peaks of fat and water, shown in Fig. 4.1, which are more prominent in the NIR and IR range due to the low interference of other absorbers.

While most research on optical tissue discrimination relies on full-spectrum measurements, multiple studies have explored which parts of the spectrum contain relevant information for this purpose. De Boer et al. [14], in particular, conducted a study on in-vitro breast samples identifying a set of eight wavelengths where statistically significant differences in the reflectance spectrum were found between healthy and tumor tissue. These were mostly in correspondence with the absorption features of the target chromophores. These results were corroborated by other studies which investigated light interaction near the selected wavelengths [16, 22, 27]. The measured reflectance is dependent on the absorption by the chromophores, but also on the scattering characteristic of the tissue, which depends on the size and quantity of scattering molecules [28, 29]. Thus, other spectral ranges able to provide information on scattering can be investigated. Kho et al. [30] highlighted the relevance of the isosbestic points, where the absorption of water and fat are the same, and can serve as reference points. Similarly, Hendriks et al. [15] proposed sets of wavelengths where the absorption coefficients of water or fat are constant. Low populated areas and absorption "dips" can also serve as discriminating factors [27] to compensate for scattering. Table 4.1 provides a summary of the most relevant wavelengths as inferred from the different studies found in literature.

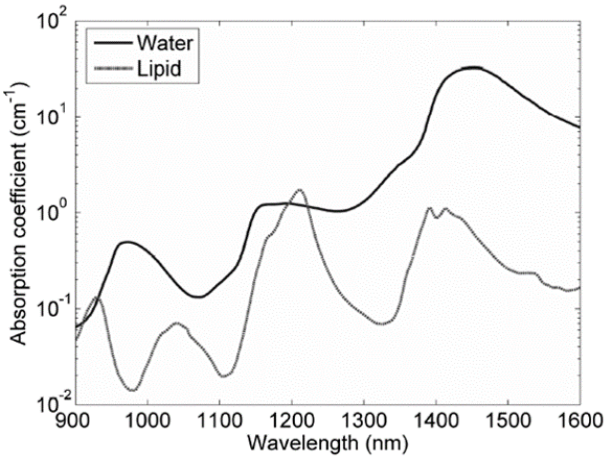

a) Water and fat absorption spectra [20].

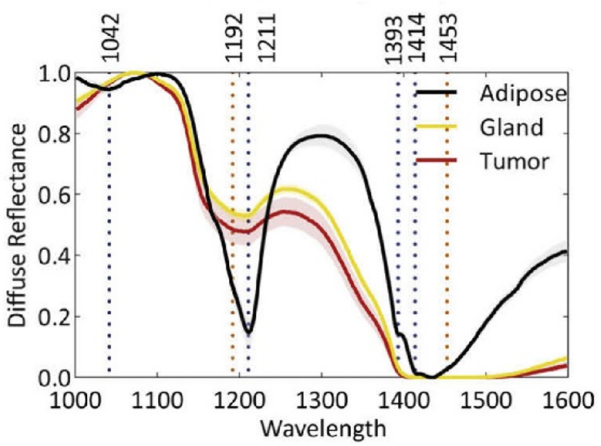

b) Example of reflectance spectra of different types of in-vitro human tissue, as measured by DRS. Adapted form [18].

Figure 4.1: The comparison between the fat and water absorption spectra, and the DRS spectra of human tissue, shows the correlation between the absorption features and the shape of the reflectance spectra. The most prominent differences in the tissues are visible at 1200 nm, where the absorption peak of fat leads to a lower detected intensity in adipose tissue.

Deboer, 2018 [14]	501 nm, 916 nm, 973 nm, 1145 nm, 1211 nm, 1371 nm, 1424 nm, 1597 nm
Bogolomov, 2016 [21]	40 nm, 1200 nm, 1300 nm, 1450 nm
Lam, 2021 [16]	930 nm, 976 nm
Kamal e Pal, 2019 [22]	850 nm, 940 nm, 1050 nm
Hendriks et al., 2013 [15]	1150.5 nm, 1251 nm, two wavelengths in the 1260-1400 nm range
Kho, 2019 [30]	910 nm, 931 nm, 1197 nm, 1222 nm, 1699 nm, 1735nm

Table 4.1: Summary of the wavelengths that have discriminating potential between tumor and healthy (breast) tissue, as inferred from different studies. The reader is referred to the cited studies for more detailed information.

4.3. Material & Methods

4.3.1. Light sources

As a preliminary test, based on the collected knowledge and availability, a wide range of wavelengths was selected to evaluate different combinations and spectral ranges. LEDs were chosen as light sources due to the low cost, and availability in multiple colors. As LEDs are incoherent light sources, their output is distributed across a range of neighboring wavelengths (half-peak width typically spanning across 20-50 nm) which is larger than most spectral absorption features. Thus, LEDs with an output close to the desired wavelengths were considered sufficient. Ultimately, seven LEDs in the 900-1500nm range were selected, with a rated power ranging from 1.5 to 9 mW: 940 nm, 1050 nm and 1200 nm LEDs were chosen in correspondence with lipid absorption peaks; 970 nm and 1450 nm for the water absorption; 910 nm as the isosbestic point, which could serve as a reference, and 1300 nm as a low-populated area which could be useful for scattering compensation.

4.3.2. Phantom preparation

Tissue-mimicking materials able to realistically reproduce the optical properties of breast tissue were produced to study light interaction with tissue. Fat content in breasts can vary from a volume fraction of up to 80% in healthy tissue, which is mostly adipose [31, 32], to values close to zero in tumor, leading to a f/w-ratio below 1 [10, 12, 29]. Thus, to study output variations depending on the f/w-ratio, phantoms which allowed for a wide range of concentrations were necessary. Particular attention was placed on reproducing the absorption profile of human tissue. Mechanical properties and physical aspects of the phantoms, on the other hand, were not considered as relevant.

Nine phantoms were made by a mixture of three main ingredients, according to the formulas developed by Azizian Amiri et al. and van Berckel [18, 29]. Pure swine lard from an online butcher (Beef and Steak, Netherlands) was used as the fat component, as animal lipid contains a fat type that is more similar to human adipose content [29]. Gelatin, a water soluble component, was used to enable different water concentrations. Salt, baking soda, and sodium benzoate (SB) were used as acidity correctors and preserving agent, respectively. EL 33 (Ethoxylated PEG-based castor oil, Chempri Oleochemicals, Netherlands) was used for the 60%-fat and 70%-fat phantom as an additional emulsifier based on the weight of lard. The mixtures were prepared and poured in identical paper cups to form discs of consistent thickness of 3 mm for the LED-test. Residual mixture was poured in other cups to form thicker samples (> 2 cm), for the DRS measurements. The exact quantities for each phantom and the fabrication procedure are detailed in Appendix C. An additional 100%-fat phantom was also produced by pouring melted lard directly into the molds, which were then refrigerated. Fig. 4.2 Shows the sample discs used for the LED-test. Throughout the document, the phantoms are identified by their fat content (in percentage), meaning that the ”60% phantom” refers to the sample with 60% fat, and 40% water.

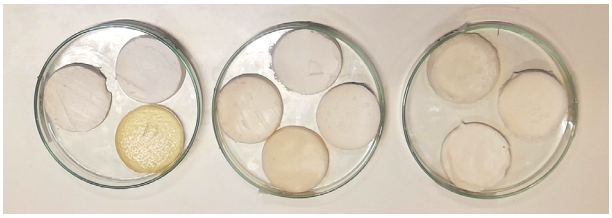

Figure 4.2: Picture of the tissue-mimicking phantoms used for the LED-tests, placed on the petri-dish for testing. Color variations between phantoms are due to different water and fat concentrations.

4.3.3. DRS measurements

Before the experiment, the DRS spectra of each phantom was acquired to investigate the optical properties of the phantoms and serve as validation of the test results.

A costume-design DRS setup (Philips research, Eindhoven) was used. The setup included a halogen broadband light source (Avantes, The Netherlands) and an InGaAs spectrometer in the 800-1700 nm range (NIRQuest, USA). The detector and light source were connected to an optical needle probe (Philips research, Eindhoven) which interfaced the DRS machine with the tissue, enabling reflectance-based measurements. The probe consisted of two optical fibers that run parallel to the needle until two apertures at the flat needle tip, at a distance of 1.2 mm. The source fiber, connected to the light source, shined light through the sample. After interaction with the phantom, light was collected by the second fiber and transmitted to the spectrometer, which measured the reflected signal. For each measurement, the machine automatically collected ten reflectance spectra and a background measurement to compensate for ambient light interference. A detailed explanation of the setup and working principle can be found in literature [12, 17].

The needle probe was fixed with a probe-holder in a vertical direction. Before measuring the phantoms, calibration was carried out using a white reflectance standard, placed at a 5 mm distance below the tip of the needle. For each phantom, three DRS measurements were performed at different locations by inserting the needle tip a couple millimeters deep into the sample. Fig. 4.3 depicts the setup used for the DRS measurements.

4.3.4. LED-test experimental setup

For the experiment, the photodetector and one LED were connected to the sensor board via coaxial cables, and placed in a transmission-based configuration: the photodetector was fixed to a manual vertical microstage (Thorlabs, USA) using a 3D printed support; the LED was fixed to a motorized linear stage (Aerotech, USA) via a second 3D printed part, as depicted in Fig. 4.4. The phantoms were placed on a petri dish in between the source and the detector. In transmission-based measurements, the distance between LED and detector has a big influence on the sensor output. Thus, the microstage was used at the beginning of the experiment to set a distance between LED and sensor. A light pressure was applied on the phantom to ensure contact with the LED, setting a source-detector separation (SDS) of 5 mm. The motorized linear stage enabled lifting of the LED for easy replacements of the phantoms, while guaranteeing a consistent SDS throughout the whole experiment.

The board was connected to a computer via USB cable for powering and data acquisition. Signals were recorded via a LabVIEW interface (LAbVIEW 2018, National Instruments, USA). To reduce electrical noise from the board, the full range of the sensor was used. The linear relationship between integration time and gain, explained in detail in Section 3.1.2, was exploited to set the gain of the TIA and amplify the signal as much as possible. The linearity between gain and *Tint* was tested with a simple, informal experiment (not reported), which concluded that any non-linearity of the TIA was negligible. As a result, two signals acquired with different *Tint* could be compared simply using a multiplying factor, equal to the ratio between the integration times. Subsequently, two different *Tint* were used for the measurements: an integration time of 200 ms was selected to achieve a readable signal when probing phantoms; a smaller integration time of 100 ms was used for the reference measurements, needed to calibrate the system. In fact, since the reference signal was taken without anything in between the light source and the sensor, the measured sensor output was much higher than that obtained with the phantoms.

4.3.5. LED-test experimental procedure

The phantoms were taken out of the fridge two hours before the measurements, to bring them to room temperature. Although all the phantoms were successful, the consistency of the 60%, 70% and 100%-fat samples was buttery and unsuitable for the test set-up, so they were not included in the LED test.

An initial background measurement was taken with no LED to investigate the influence of external lights, but as the external interference value was always zero, no further background measurement was recorded. One LED at a time was connected to the board and used in combination with every phantom. Before the measurements with

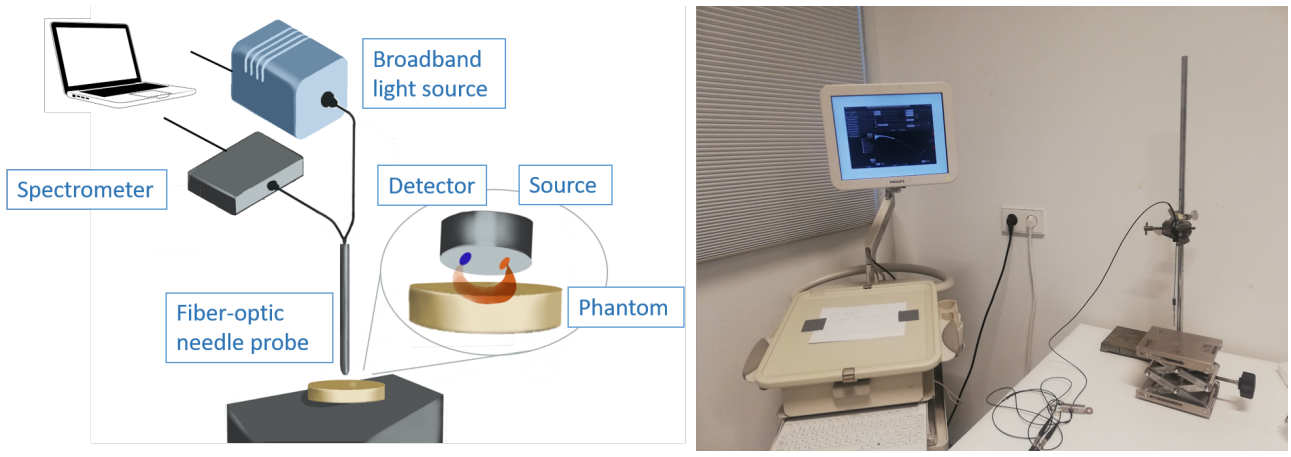

Figure 4.3: Schematic representation and picture of the DRS setup. The final setup included the DRS machine connected to the needle probe via optical fibers; a vertical holder for the needle and a manual linear stage for positioning of the samples.

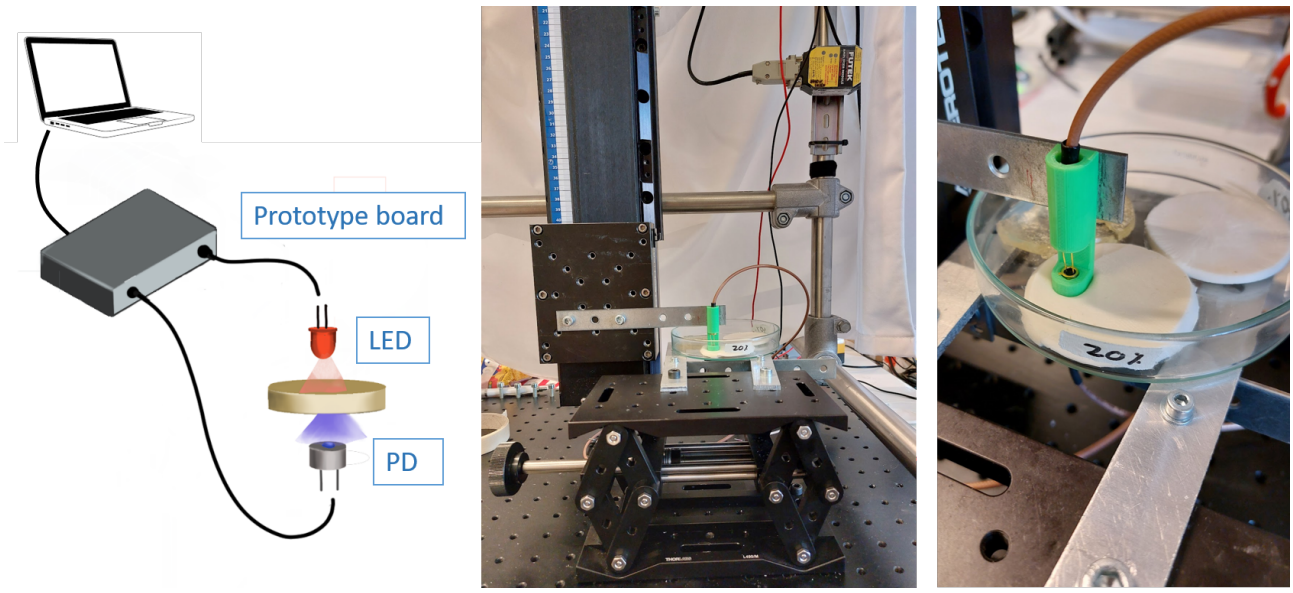

Figure 4.4: Schematic and pictures of the transmission-based test setup. The phantom is placed on a support mounted on the manual precision microstage, over the photodetector (PD). The 3D-printed LED support (in green) is mounted on the motorized linear stage. The sensor and LED are connected via coaxial cables to the sensor board.

phantoms, the driving current of the LED was set via PWM so that the reference signal was as high as possible within the sensor's range. To perform a measurement, LabView data acquisition was enabled for ten seconds at a time, leading to about twenty samples per measurement. For each LED, four reference measurements were performed, followed by four measurements for each phantom at different locations.

4.3.6. Data analysis

Representative parameter

Throughout the experiment, the percentage of fat in the phantoms was used as the representative parameter instead of the f/w-ratio, as it was considered more intuitive to interpret. Such decision is justified as water and fat are the main constituents of the phantoms. Thus, the water concentration can be directly inferred from the fat content, and the f/w-ratio can be calculated as *Fat%/(100 – Fat%).*

DRS measurements

The measurements of the spectrometers were processed using a Philips custom-developed Matlab-based software. The software fitted the spectra with the analytical model developed by Farrell et al. [33] to estimate fat and water concentrations, as well as the scattering and absorption profile of the phantom. It only allowed fitting from 1000 nm, so the raw spectra (800-1700 nm) were also plotted. Qualitative analysis of the plots was performed to compare the different optical spectra between each other and in relation to the LED-test results. More information on the software and estimation model can be found in previous publications [11, 12, 17, 20] The estimated fat content of each phantom was also calculated from the fit results to check the actual composition of the phantoms. The fat percentage for each replicate measure was obtained by multiplying the total fat and water volume fraction with the fat fraction: *(F + W)∗F/(F + W)∗100.*

LED-test

Matlab (MathWorks vR2 021a, USA) was used to analyze the data. Pre-processing consisted in plotting the raw data to check for any unexpected value and outlier. A missing measurement for the 1300nm LED was replaced by a NaN vector for the analysis. Then, the measurements were cropped to obtain the same amount of samples for each. The mean and standard deviation of every measurement was calculated. This process resulted in a total of 224 data points (4 measurements x (7 phantoms + 1 reference) x 7 LEDs). The mean value and standard deviation was calculated for each LED-phantom combination, and used along all the replicates for descriptive analysis. To compare the response at different wavelengths, for each phantom-LED combination the intensity (*I*) was normalized based on the mean reference of the LED, to obtain a normalized intensity (*In*) in the 0-1 range, according to the formula:

$$I_{n,\lambda}^{fat\%} = \frac{I_{\lambda}^{fat\%}}{I_{\lambda}^{\text{ref}}} \quad (4.1)$$

Line plots were used to visualize the measured "spectra" for each phantom, and qualitatively compare them with the DRS. To evaluate the influence of fat/water on the measurements, the shapes of the spectra corresponding to different phantoms had to be compared. Thus, the data was scaled at the different wavelengths (λ_{ref}) to easily visualize the difference in response between wavelengths and correlate it to the sample composition. The scaled intensity S was obtained, for each phantom data, by dividing all the values by the value at the reference wavelength ($I_{n,\lambda ref}$). The scaled intensity value at the reference wavelength (=1) was subtracted to the others for an easier comparison:

$$S_{\lambda}^{fat\%} = \frac{I_{n,\lambda}^{fat\%}}{I_{n,\lambda ref}^{fat\%}} - S_{\lambda ref}^{fat\%} \quad (4.2)$$

Through this transformation, the scaled intensity actually represents the ratio between intensities at two wavelengths. This quantity was considered able to represent differences in the spectral shape between phantoms, but the choice was arbitrary, so other quantities and transformations may have been chosen to compare the results.

Qualitative analysis of a number of graphs was performed to interpret the results. Finally, a least-square linear regression was performed using the Matlab function *polyfit* to determine the relationship between the measured scaled intensity and the fat content of the phantoms. The R^2 value and plot of the residuals were used to evaluate the goodness of fit.

4.4. Results

4.4.1. DRS measurements

The mean DRS spectra of each phantom material can be found in Fig 4.5, while Fig 4.6 represents the results of the fit model, in terms of total estimated reduced scattering coefficient and absorption coefficient. The replicate measurements differed in intensity, but the shape remained consistent. The 100% phantoms displayed a higher variability compared to the other phantoms, which was reflected in the scattering coefficient but not in the absorption spectra. Clear differences were visible for all parameters between phantoms. In

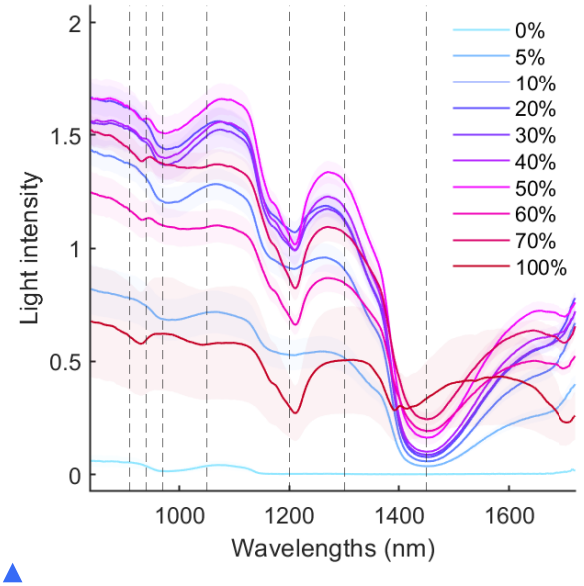

Figure 4.5: For each phantom, the plot shows the mean spectra ± SD of all replicates measurements performed at different locations. The dashed lines represent the wavelengths of the LEDs used for the test.

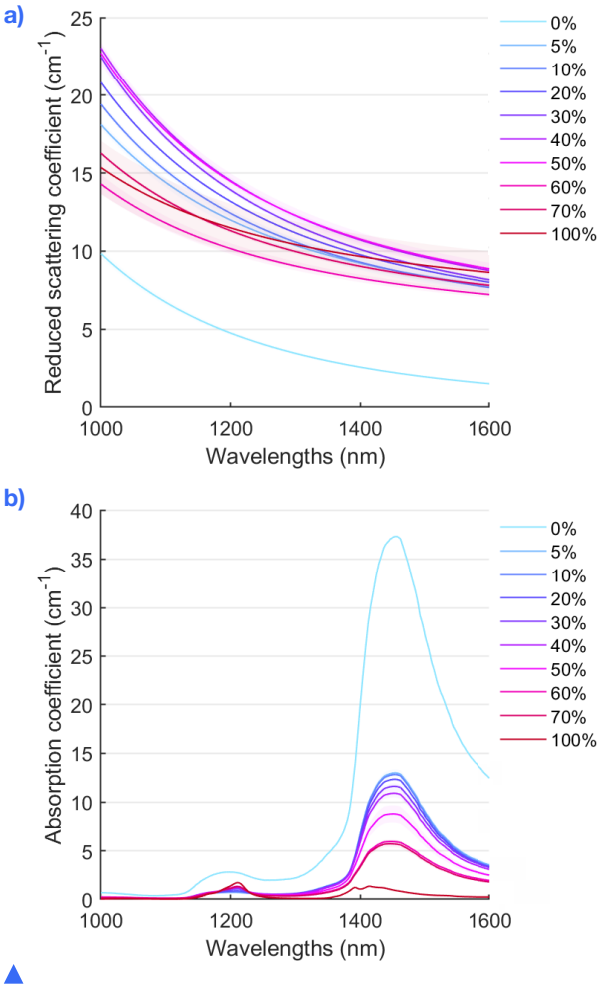

Figure 4.6: Mean reduced scattering (a) and absorption (b) ± SD of each tissue-mimicking phantom, estimated from the reflectance spectra via the dedicated Matlab software.

particular, as expected, a more prominent dip was present for higher fat percentages at 1200 nm. The response of the 0% sample was very different from the others, presenting an intensity below zero at high wavelengths. The shape of the absorption profile remained consistent within phantoms, with the height of the peak around 1450 nm increasing with water content, while the (smaller) peak at 1211 nm was proportional to the fat percentage. The scattering amplitude increased with fat content until 50%, while the 60%, 70% and 100% phantoms showed lower values. The latter also presented a reduced scattering slope. The 0% phantom curve was the steepest.

Table 4.2 reports the mean estimated fat content for each phantom, based on the fit result. The estimated value was lower than expected for all phantoms, with an average offset of 5% (expected value – mean value). For the 60% and 70% phantoms, the algorithm underestimated the fat content attributing both around 53% fat percentage.

Expected Fat %	Mean Estimated Fat %
0	0.00 ± 0.00
5	2.45 ± 1.22
10	7.31 ± 0.55
20	15.66 ± 0.47
30	27.20 ± 2.36
40	34.10 ± 1.57
50	47.60 ± 0.98
60	53.08 ± 2.30
70	53.99 ± 1.35
100	98.97 ± 0.13

Table 4.2: Mean fat content estimated for each phantom from fitting of the DRS reflectance spectra, compared to the expected fat % according to the formula used for the fabrication of the phantoms.

4.4.2. LED-test

The recorded signals were stable, characterized by an SNR above 20dB, and spanned across the whole sensor's spectrum (0-1.2 V). The 0% phantom led to the largest amplitudes, with recorded average voltage values between 1199.12 ± 1.56 and 246.91 ± 0.92 mV across the different wavelengths. All the other signals had much lower average values, between 85.70 ± 0.48 mV and 0.69 ± 0.07 mV. The lowest absolute voltage levels were obtained with the 1450 nm LED, for which all the recorded signals were below 14.65 mV. After averaging and calibration, which consisted in normalizing the signals based on the reference measurements of each LED, the intensity values at different wavelengths were comparable. Fig. 4.7 reports the results of this transformation, in the form of discrete transmission spectrum. Aside from the clear difference in absolute intensity between the 0% phantom and the rest of the samples, the main visible effect was the reduction in detected intensity as fat percentage increased, at all wavelengths.

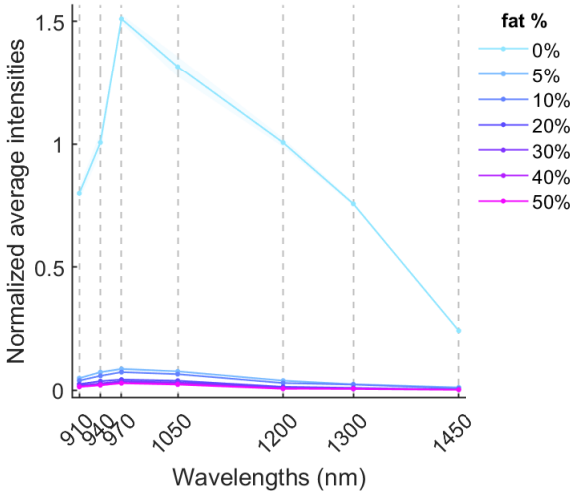

a) Full range discrete spectra.

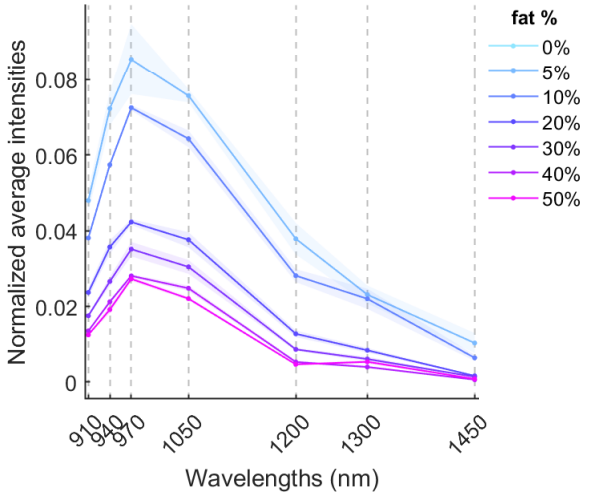

b) Zoomed-in discrete spectra.

Figure 4.7: Average intensities (±SD) normalized by the reference measurement for each LED. a) shows the whole sensor's range, including the results of the 0% phantom, while b) is zoomed-in on the discrete spectra of the phantoms with higher fat percentages.

At a first analysis of the spectral shape compared to expected values from the full spectrum measurements, the characteristic “dip” at 1200 nm was not visible. As two different 1300 nm LEDs were available, the test was repeated the following day with both 1300 nm LEDs (1300E, used in the first test, and 1300L. Thorlabs, USA). The test procedure was the same, but the exact SDS could not be reproduced. As a result, the detected values were not directly comparable to those of the first test. The 1200 nm was thus also included in the test as a reference. Fig. 4.8 reports the results of the repeated test, after calibration.

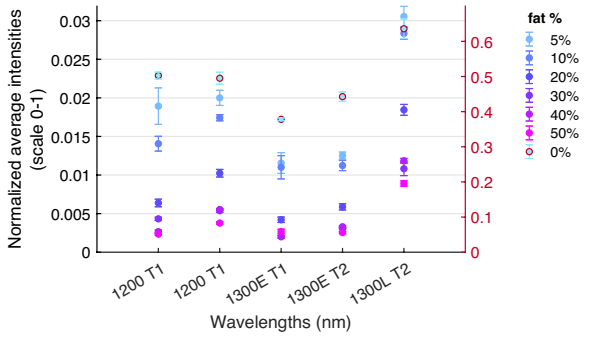

Figure 4.8: Results of the repeated test with the two different 1300 nm LEDs. The graph reports the intensity values normalized by the reference signals obtained in the two consecutive days. “T1” refers to the first, complete, test; while “T2” refers to the results of the repeated test. The 0% values are shown on a different scale (right y-axis) to fit in the plot.

The results for the 1300E LED were relatively consistent with the previous day, considering that a slightly different SDS was used, but the 1300L LED led to much higher measured intensities compared to 1200 nm. This was consistent with the expected values according to the spectra, and thus these values were also taken into account for the rest of the analysis. To compare the results of different LEDs, the discrete spectra were separately scaled at all the wavelengths and plotted to visually investigate possible trends. Scaling at 1200 nm led to interesting results for both the first test and the test repeated with the new 1300L LED, plotted in Fig. 4.9. Compared to 1200 nm, the LEDs between 910 nm and 1050 nm used in the first test, and the 1300L LED used in the repeated test showed a consistent increase in slope at higher fat content. The same transformation applied to the full spectral data led to similar results.

The 970 nm LED and the 1300L nm LED specifically displayed a recognizable gradient. Fig. 4.10 shows the scaled data at 970 nm and 1300L nm in relation to the fat percentage.

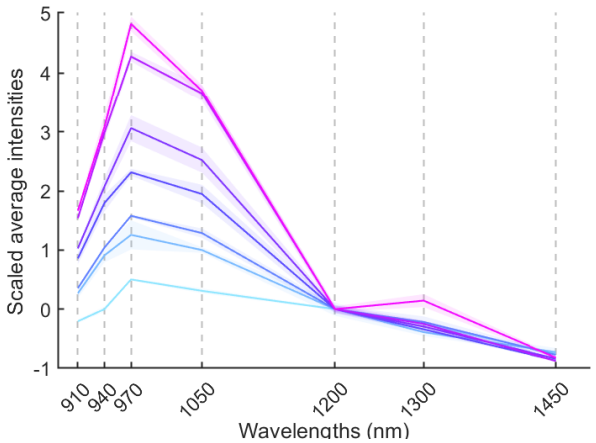

a) Results of the first, complete, test

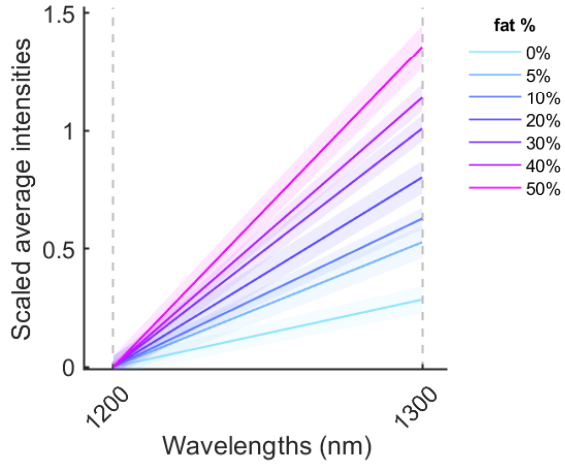

b) Results of the test repeated with the 1200 nm LED and the 1300L nm LED.

Figure 4.9: Mean and standard deviation of the discrete transmittance spectra, scaled at 1200 nm. As the test was repeated with the 1200 nm and two 1300 nm LEDs, b) shows the promising results obtained with the 1300L LED.

Despite the high variability between replicates, both graphs showed an approximately linear relationship. Linear fitting of the data led to two equations describing the fat-intensity curve at 970 nm and 1300 nm, respectively. The fat-intensity curve at 970 nm was described by $y=0.08489x+0.682$, with an R^2 value of 0.95. The equation for the 1300 nm curve was $\boldsymbol{y}=0.01986x+0.3843$, with an R^2 value of 0.88. The residuals of both regression models were quite evenly distributed around 0.

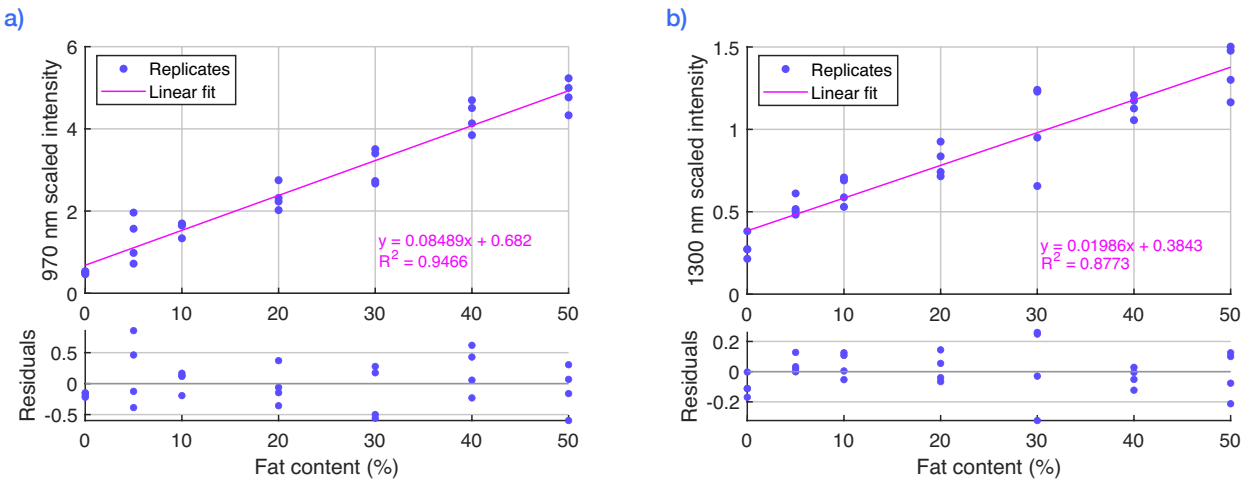

Figure 4.10: Scaled intensities at 970 nm (a) and 1300 nm (b), plotted against the fat percentage. The blue dots represent all the replicate measurements. The pink line represents the result of the linear fit. The residual of each linear regression are graphed in the bottom plots.

4.5. Discussion

4.5.1. DRS measurements

The results of the DRS spectra served to characterize the phantoms, and later to compare them with the results of the LED-test. The absolute intensity of the spectra is dependent on many factors and is not of particular interest for this research. The spectral shape, on the other hand, contains information regarding the tissue properties. Generally, the obtained spectra were consistent with the literature. The 0% phantom was not fully measurable due to substantial light dispersion in the tissue, which led to a very small reflectance signal. This is explained by the high water content, which has high absorption values in the NIR-IR range, and the low reduced scattering caused by the absence of fat, which is the main scatterer in the sample [12].

The height and shape of the absorption spectra were generally comparable to those of human tissue, when considering healthy adipose tissue with fat percentages above 50%, and tumor tissue around 20% [18]. On the contrary, both the amplitude and slope of the scattering coefficient seemed higher than in real human tissue. In breast tissue, studies reported that the scattering amplitude normally ranges from about 5 cm^{-1} in adipose tissue to 8 – 15 cm^{-1} in malignant tissue [12, 26, 34]. Few higher values have been reported; For example, Bydlon et al. measured an amplitude of up to 25cm–1 in invasive ductal carcinoma [35]. The scattering curve was steeper for lower f/w-ratios, in line with the properties of human and animal tissue [12, 18, 22], with the exception of the 60%, 70% and 100% samples. The scattering coefficient is an indicator of the quantity and size of the scattering molecules present in the tissue [29]. Thus, the difference in scattering between the phantoms and human tissue could be attributed to the size of the scattering particles, which depends on the fabrication procedure and materials. Van Berckel [29] and Nachabé [12] conducted an in-depth investigation into the influence of different tissue-mimicking fat emulsions on the optical properties of phantoms.

The 60% and 70% samples, fabricated with an additional emulsifier, showed a scattering profile more similar to that of the swine lard, which is closely related to human adipose tissue [12], but their fat content was significantly underestimated by the mathematical model. Although small differences from the desired quantities may be connected to inaccuracies during the fabrication process, those do not explain this level of variation. A hypothesis is that the emulsifier modified the optical properties of the phantoms in a way that is not consistent with human tissue, for which the model is calibrated. Other causes for the deviation of the estimated fat fraction from expected values may be the small SDS, as the Farrel model is less robust for reduced sensor-detector distances [36], or the temperature of the phantoms, which was not constant; as the absorption coefficient of water is temperature dependent, it may have impacted the results [11]. For the purpose of this test, the resemblance to human tissue was not crucial, but will need to be considered when translating the method to real tissue.

4.5.2. Sensor performance

Overall, the performance of the sensor board was suitable for the test. However, the wide dynamic range was inherently a limitation of the measurement method and test setup: when signals with such different amplitudes need to be measured, noise optimization can only do so much. The reference signal and 0% phantom were the limiting factors in this case. The intensity of the reference signal was already limited by reducing the gain of the amplifier. Possible improvements in the setup could include adapting the gain to the amplitude of the signals via the integration time, or increasing light dispersion with different materials and phantoms, to obtain signals that are roughly in the same amplitude range. Once this is obtained, the signals can be amplified even more, to enhance the SNR.

The "repeated test" with the 1300 nm LEDs showed a very important dependency of the system to the choice of light source. The new 1300 nm LED (1300L) led to significant findings, so the results of the repeated tests were used for the rest of the analysis. However, the nature of the difference between the two LEDs was not clear, and although it is likely due to the technical specifications of the two LEDs, this issue should be investigated further. The differences between measurements with the same LED over the two repeated tests were partially expected because of the slightly different SDS that was used. For this reason and due to the low number of samples, these differences were only assessed qualitatively. However, these variations may also be associated with other factors, so a larger study and statistical analysis should be performed to assess the cause of this variability.

4.5.3. f/w-ratio effects on the measured values

The first noticeable effect was the reduction in absolute intensity when the fat content was higher. This was in agreement with the findings of Bogolomov et. al [27] and Kamal and Pal [22], who found significant differences in the reflectance signal amplitude between healthy and cancerous liver and breast tissue, respectively. The discrete spectra shapes were also consistent with the results of Bogolomov et. al, showing a similarity between the results on tissue-mimicking phantoms, and measurements on real human tissue. This is a relevant finding, as it was partially validated by previous studies, but is not necessarily usable in practice. The absolute intensity measured by the sensor highly depends on external factors such as the power output of the light source or the SDS. Furthermore, a gradual increase of the scattering amplitude was also observed for higher lipid content. In transmission measurement, higher scattering means that less light reaches the sensor opposite the light source, so a smaller intensity is detected. This would explain the intensity gradient seen with increasing fat content, which is then dependent on scattering only, rather than the sample's chromophore composition.

The shape of the spectra, on the other hand, is more consistent within different experimental setups and reflects the differences in absorption and scattering of the chromophores in different zones of the light spectrum. Thus, comparison between values at different wavelengths can result in a more robust optical detection method. The scaled intensity (ratio of intensities between the wavelength of interest and a reference wavelength) was calculated to compare the spectral shapes. However, this choice was arbitrary and other transformations may also lead to relevant results.

Scaling by the intensity at 1200 nm showed that there were significant differences in the intensity measured at different wavelengths, both within the same phantom and compared to other fat percentages. This finding answered the first research sub-question. Furthermore, it was found that the intensity ratios between 970nm and 1200nm, and 1300nm and 1200 nm, were linearly correlated with the fat percentage. The R^2 value of both fitted functions was close to 1, indicating a good fit. 970, 1200 and 1300 nm were thus identified as the most relevant wavelengths, answering the second research sub-question.

The importance of the 1200 nm wavelength for the purpose of f/w-ratio estimation was already mentioned in Section 4.2, due to the presence of an evident peak of lipid absorption at 1211, nm along with the adjacent isosbestic points. Kho et al. [30] demonstrated a method to estimate fat content in breast tissue based on the slope around 1197 nm, calculated at a distance of 10 nm. Even when larger distances from the reference are considered, around this range the absorption of water is approximately constant. Assuming that scattering had a negligible influence, and that water and fat were the only two significant absorbers in the probed optical range, any change in the measured signal was purely due to a change in lipid content. This would explain the scaled intensity gradient seen between 1300 nm and 1200 nm. Furthermore, at 970 nm, the absorption of fat presents a dip, which

corresponds to an equally high water absorption peak. Compared to the reference isosbestic point, the linear relationship of the fat-intensity curve at this point is also explained. This finding should be validated to discover if these relationships remain consistent in different scenarios. To answer the final research sub-question, once the result are validated, a measurement carried out with the multi-wavelength device, probing the tissue at the relevant wavelengths, would result in intensity values which can be transformed to obtain the scaled intensity. By applying the formula of the linear function, the latter could then be directly converted into a value representing the fat and water content of the phantom. Based on discrimination algorithms such as those proposed in literature [12, 14], the measured intensity could be attributed to specific tissue types such as tumor or adipose tissue.

Throughout this study, the terms fat percentage, fat content, and fat concentration were used interchangeably. The fat percentage was used as representative optical parameter instead of the f/w-ratio for easier interpretation of the results. This choice was justified as fat and water were the only relevant tissue components. In fact, gelatin does not have a significant influence on the optical response of the mixture, and the other ingredients were in negligible quantities. However, in reality, tissue has many constituents, so the mentioned quantities would take on different meanings. As a result, the water content could not be directly inferred only from the fat content in the tissue, and the f/w-ratio would also be calculated differently.

4.5.4. Influence of scattering

To apply the proposed measurement method, two assumptions were mentioned in the previous section: scattering had a negligible influence, and water and fat were the only two significant absorbers in the probed optical range. These assumptions are quite strong. However, in reference to human tissue, the assumption that water and fat are the only absorbers is partially supported by literature: water, lipid and collagen are the main absorbers in the NIR range, but it was demonstrated that including the absorption spectra of collagen is not necessary for tissue discrimination [10, 34]. Concerning scattering, multiple studies have demonstrated significant differences in reduced scattering amplitude and slope between healthy and tumor tissue [10, 12, 20, 34]. However, the slope of the scattering profile is relatively low, meaning that differences between the coefficients evaluated at multiple wavelengths have a small influence on the overall shape of the reflectance spectrum. Lam et al [16], specifically, demonstrated that the scattering parameter is negligible for f/w-ratio estimation via DRS, and can be considered constant in the 900-1000 nm range. In the context of this experiment, a wider wavelength range was examined, between 910 nm and 1450 nm. The assumption on scattering was violated, as the slope of the scattering curve was found significantly different than zero for all phantoms. Nonetheless, the tests showed the presence of a linear relationship between fat content and scaled intensity, supported by the study by Kho et al. [30], mentioned previously.

The experiment was designed to investigate the f/w-ratio as the only discriminator between malignant and healthy tissue. To build a discrimination method based on this parameter, we need to evaluate the effective influence that other parameters play in the results of the test. For instance, the estimated scattering coefficient displayed a relatively consistent increase in slope depending on the fat percentage, which may also have contributed to the observed linear fat-intensity curve. This parameter is also considered relevant to estimate chromophore concentrations, as it is necessary for the application of the Farrel model [33, 35, 36]. Furthermore, as mentioned by Nachabé et al. [11], lipids are biological scatterers, meaning that the scattering coefficient can carry information regarding the fat content. Thus, two approaches may be considered to design a tissue discriminating method for breast tissue:

One option is to find a way to compensate for scattering, so that the measurement is only dependent on the chromophore content. It is then possible to apply a discrimination algorithm based on the f/w-ratio to distinguish between tissue types. This approach entails a trade-off. The resulting optical detection method is more robust against differences in scattering due to probing location, tissue type and intra-patient variability, at the cost of the loss of the information on lipid content contained in the scattering profile.

A more empirical approach, on the other hand, can exploit the influence of scattering for tissue discrimination. In this case, studies should be carried out directly on real human breast tissue to observe the exact fat-intensity relationship. Although this method is theoretically simple, a large amount of data and samples should be examined to ensure that the method holds for different patients, body locations, light conditions, etc. Furthermore, the measurements should be

performed on animal or human tissue, or very realistic phantoms, which could be a hurdle for practical implementation. Future studies should carefully consider both possibilities to increase the chance of finding an effective and robust optical discrimination method for breast tissue.

In the context of this graduation project, possible methods to compensate for scattering were explored as a side research, which served mainly to understand the results of the tests and propose alternatives to the relevant quantity extracted from the optical signal, in the form of intensity scaled at 1200 nm. This study is only a preliminary investigation into the influence of scattering on multi-wavelength tissue measurements, and didn't lead to any conclusive results. The resulting ideas and theories are thus presented in Appendix D.

4.5.5. Limitations

Although the results of the study were promising, certain limitations were associated with the specific setup and experimental design.

The main limiting factor of this study was the small sample size and variability of the measurements. The former limited the power of any conclusion due to statistical significance. The latter, on the other hand, directly influenced the results and possibly hindered practical implementation of the optical detection method. Specifically, even if the relationship between lipid content and sensor's output is a well defined linear function, a single measurement taken on a non-characterized tissue sample may lead to inaccurate estimation of its composition.

A source of variation was certainly the transmittance-based setup, due to which the measured light intensity was highly dependent on the SDS. Measures were taken to provide a consistent SDS through the whole experiment, but the inhomogeneity of the phantoms and their thickness led to low precision. Other effects such as swelling of the samples due to temperature, or positioning of the LED and sensor in the holder, may have influenced the sensor's output.

Another possible confounding factor was the temperature of the phantom. Although the samples were all removed from the fridge simultaneously, variations in temperature between them, or throughout the experiment, may have influenced the absorption of water, and thus the measured intensity.

Finally, very high and very low values of voltage had to be detected with the same system. Very low voltage values were more subject to inaccuracy and errors due to the electrical noise, which had similar amplitudes.

5.

Validation Test

5. Validation Test

Regardless of the high variability of the results, and small sample size, the first test showed promising results for the purpose of fat and water content estimation in tissue mimicking phantoms. In particular, the ratio in measured intensity between 970 and 1200 nm, or 1200 and 1300 nm, changed linearly depending on the f/w-ratio of the probed tissue. Two different linear functions were identified for the comparison at 970 nm and 1300 nm, respectively. The exact factors that determined the coefficients of these functions were not known. To devise a robust method for the optical estimation of fat and water concentrations in tissue, these elements were further investigated with a second test.

Two primary and one secondary research sub-questions were formulated for this purpose, as already mentioned in Section 2.2:

1. If the test is repeated, are the results consistent with the first test?

2. Is the identified relationship between fat content and measured intensity well defined?

3. Is the identified fat-intensity relationship robust against scattering?

Question 1 and 2 investigated whether the results obtained in the first test were purely circumstantial, or accurately represented the optical behavior of the phantoms. Thus, the initial LED test was repeated under similar conditions for the relevant wavelengths, together with the DRS measurements.

The secondary research question emerged from one observation: although the initial experiment was mainly focused on the differences in absorption between fat and water, scattering may have had a more relevant impact on the measured values than initially estimated. Studies have confirmed that differences in the scattering behavior of healthy and tumor tissue could be used as a discriminating factor [10, 20, 34], but this effect may be detrimental for the purpose of f/w-ratio estimation. In the context of this experiment, the mentioned issue was addressed by including two additional phantoms with a different scattering profile.

In this chapter, the first section explains the formula and production process for the new phantoms, along with the improvements realized on the test setup and procedure to address the limitations of the first test. Then, the results are presented and compared to the first test. Finally, the combined results are discussed to answer the research questions.

5.2. Materials & Methods

5.2.1. Phantom Preparation

For the validation test, a wide range of fat percentages was included to compare the results of the two tests. After an evaluation of the previous phantoms, it was found that the scattering profile of the phantoms was not representative of human breast tissue. As phantom fabrication was not the aim of this study, only minor modifications were applied to the formula in the hope of improving the samples. Particularly, preliminary tests showed that the addition of transglutaminase (TG), an enzyme used for the crosslinking of gelatin, might result in more durable phantoms with a flatter scattering profile, closer to that of human and porcine tissue samples. On the contrary, the use of an additional emulsifier (EL 33) affected the f/w-ratio estimation of the Farrel model, so it was discarded. The final formula included swine lard, water, gelatin, SB, TG, and baking soda. The fabrication procedure and quantities were identical to those already described in Appendix C. TG was added before using the electronic mixer in a quantity corresponding to 2.5% of the water volume. 7 phantoms were manufactured in the range of 0% - 60% fat content, in 10% intervals.

The secondary objective of the study was to evaluate the impact of scattering on the measurements. Lipids can be made up of different types of fat, which are associated with different scattering and absorption behaviors. Since butter and margarine have a different fat composition compared to animal lard [20], over-the-counter butter with a 82% fat content, 32%-fat margarine (Jumbo, Netherlands) and pure lard (100% fat) were melted and poured into the molds without further processing.

To guarantee phantom homogeneity and a constant thickness of 2 mm, dedicated molds were fabricated with 3D printed supports and microscope-grade glass slides. The reduced thickness of the glass (0.17 mm) compared to the petri dish also increased the intensity of the detected signal, and protected the phantoms from contact with the air and LEDs. The glass supports that contain the phantoms are depicted in Fig. 5.1.

5.2.2. Experimental Setup & Procedure

The experimental setup, test procedure and processing of the data for both the LED and DRS measurements remained consistent. The new sample holders allowed for easy replacement by sliding the phantoms between the LED and sensor, so the SDS was set at the beginning of the test and remained fixed throughout the whole experiment.

Based on the results of the first test, a subgroup of wavelengths was selected: 970 nm, 1200 nm and 1300 nm were included to test the linear relationship. 910 nm was maintained to further investigate the scattering compensation method proposed in Appendix D. The results concerning this wavelength are only reported to the extent that is relevant for the validation test, while a more detailed analysis is reported in Appendix D.

Compared to the first test, the subgroup of LEDs had a relatively similar power output, so PWM current control was not used, as it was considered an additional source of electrical noise. The appropriate current level was selected by connecting the coaxial cable to the 46 mA or 100 mA current output of the board. The integration time was set to 50 ms for the reference and the 0% signal, while 300 ms was used for the other measurements. Hold and reset periods of 100 ms guaranteed passive cooling of the LEDs to avoid temperature drift. The experiment was carried out over two days to produce a larger sample size: four measurements per LED-phantom combination were taken on the first day with the exception of

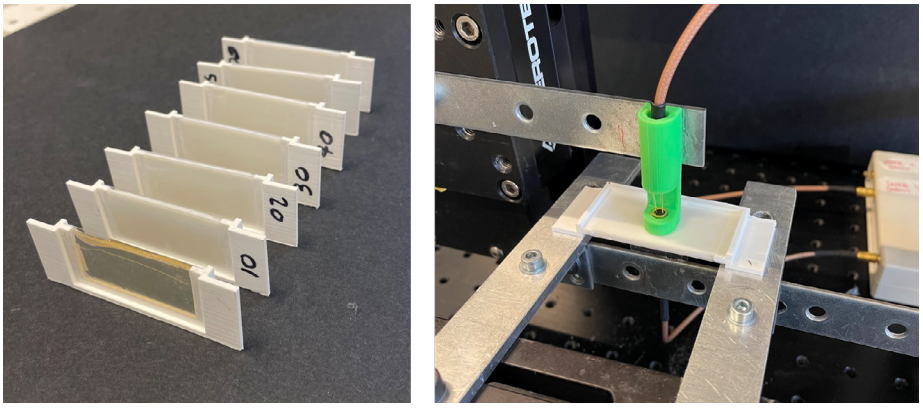

Figure 5.1: Pictures of the custom fabricated phantom holders made of glass slices. The sample mixture is poured in the molds and left to solidify prior to the experiment. The phantom holder is then placed between the 3D printed LED support and sensor support for the measurements.

the 0% phantom, which had to be refabricated. A second set of six measurements per combination was taken on the second day in the same conditions. The DRS measurements were performed on the second day following the procedure described in Section 4.3.5.

5.2.3. Data Analysis

Data analysis of the DRS results was carried out similarly to the first test, to obtain the raw reflectance spectra. Based on those, the estimated reduced scattering and absorption coefficients, and the estimated fat content, were used as a way of checking the phantoms' composition and to validate the LED-test results. The LED-test, on the other hand, had the specific goal of validating the findings of the previous experiment, in which a proof-of-concept method for fat estimation was developed based on the linearity of the fat-intensity curve. For this purpose, the measurements acquired during the two consecutive days were grouped and transformed to obtain the fat-intensity curves at 970 nm and 1300 nm: the data was calibrated against the reference signal and scaled at 1200 nm; then, a least-square linear regression was performed on the scaled intensity values to evaluate the linear relationship with lipid content and compare it with the equations found in the proof-of-concept test. Afterwards, the results were investigated in more detail to understand the source of variability of the data-set: the values from the two consecutive days were studied independently and qualitatively compared to the DRS spectra. As previously mentioned, the results of the measurements conducted with the 910 nm test only served for the additional study on scattering conducted in Appendix D, and were thus not included in this analysis.

5.3. Results

5.3.1. DRS measurements

Fig. 5.2 shows the DRS spectra scaled at 1200 nm. From qualitative analysis of the plots, the mean spectra of the new phantoms were generally consistent with the expected results. The new 60% phantom, fabricated without extra emulsifiers, led to an optical response more comparable to that of the other spectra. The 82% measurements had a higher variability compared to the rest. These results were reflected in the estimated reduced scattering and absorption coefficient, shown in Fig. 5.3.

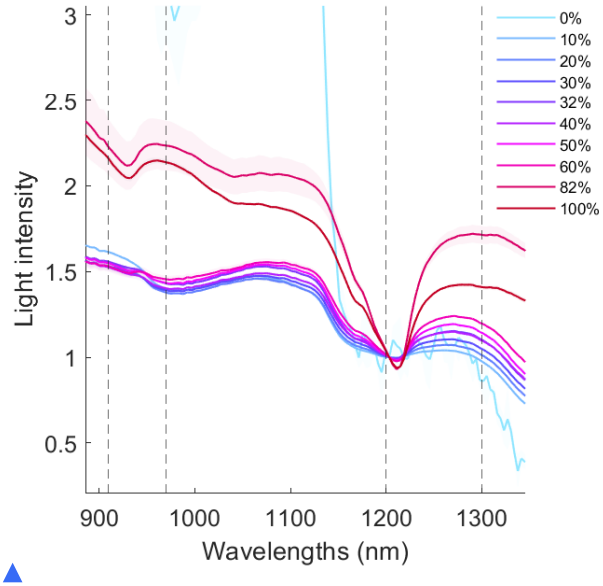

Figure 5.2: Mean DRS spectra ±SD of all replicates, scaled at 1200 nm. measured with DRS. The 0% line was cropped, as the DRS measurement was inaccurate. The dashed lines represent the wavelengths of the LEDs used for the test.

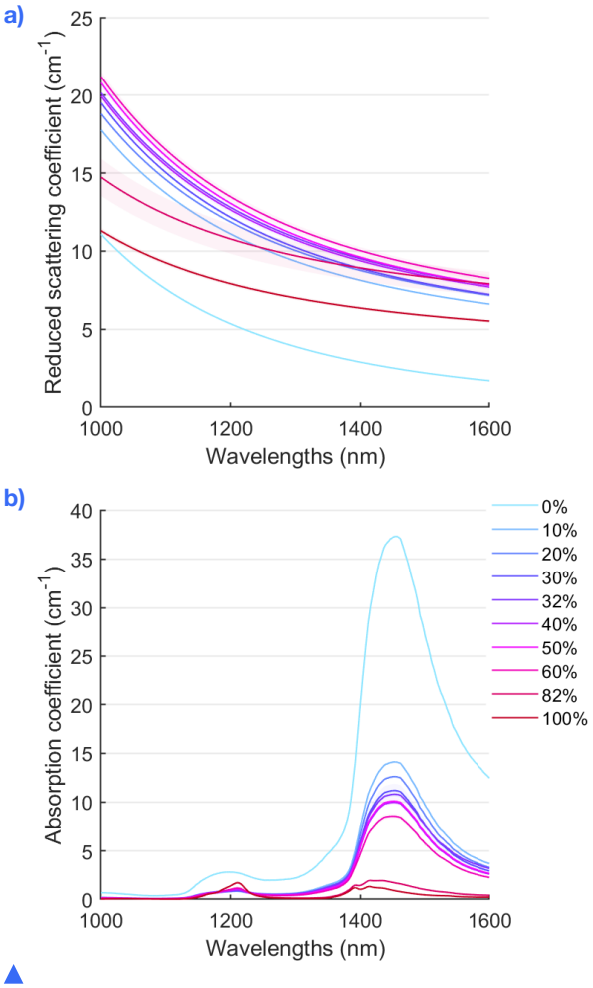

Figure 5.3: Mean reduced scattering (a) and absorption (b) ± SD of each tissue mimicking phantom, estimated from the reflectance spectra via the dedicated Matlab software.

The scattering slope and power of the butter and lard samples were lower compared to the other scattering profiles, with the 82% butter displaying a larger variability. For the other samples, the slope was relatively constant, and the intensity increased with the fat content. The 32% margarine scattering line was the exception, being higher than the 40% sample. The absorption profiles were consistent with previous findings, although the overall SD was higher and the 1450 nm absorption peak of the 50% sample was slightly steeper than the 40%. Regardless of the addition of TG, the reduced scatterings did not show any significant differences from the previous experiment.

Table 5.1 reports the fat-water ratio estimated by the model for each phantom. Compared to the expected values, there was a relatively large mean absolute offset of 7.7%. Above 10%, the fat content of all samples was significantly underestimated, with the exception of the butter sample, which was estimated at 96.55%, and 100%, which was accurate. The offset was relatively consistent between measurements, so it was assumed that the relationship between different spectra was not significantly affected. From these results, it was impossible to pinpoint whether the underestimation was caused by an issue of the estimation model and DRS measurements, or by an actual deviation in the phantoms' composition from the desired values. Thus, for the rest of the analysis, the expected fat content values were used as reference. Evaluation of the impact of this difference on the results is left for the discussion.

Expected Fat %	Mean Estimated Fat %
0	0.00 ± 0.00
10	9.58 ± 0.24
20	14.67 ± 0.91
30	21.71 ± 0.73
32	24.30 ± 1.19
40	29.27 ± 0.71
50	36.38 ± 0.68
60	44.34 ± 1.32
82	96.55 ± 0.25
100	99.08 ± 0.02

Table 5.1: Mean fat content estimated for each phantom from fitting of the DRS reflectance spectra, compared to the expected fat percentage according to the formula used for the fabrication of the phantoms.

5.3.2. LED-test

Overall, the performance of the sensor board was consistent with the previous test. Thanks to the smaller SDS, the sensor's output was larger, so a smaller *Tint* was used. The 0% and reference measurements were taken with the same *Tint* due to the similar voltage amplitudes. Therefore, the gain for the rest of the signals could be higher and improve the SNR. The minimum detected signal was 38.61±1.23 mV, against the 0.69±0.07 mV of the proof-of-concept experiment. The total maximum detected voltage was 1172.48±1.97 mV. Fig. 5.4 Shows the intensities measured at 970 nm and 1300 nm after scaling at 1200 nm, plotted against the fat content of the phantoms.

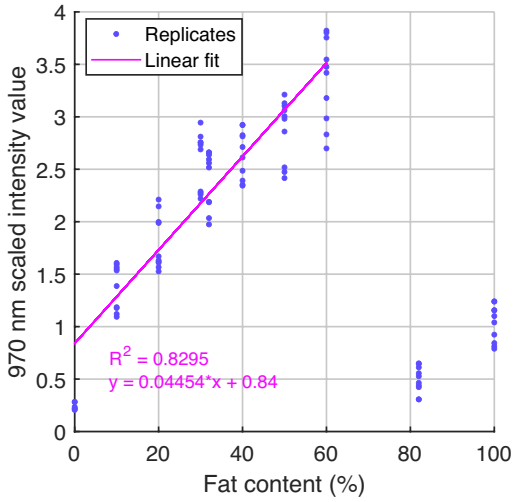

a) Fat-intensity curve at 970 nm.

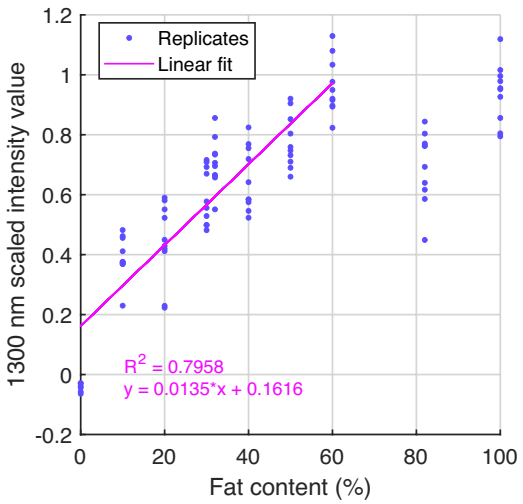

b) Fat-intensity curve at 1300 nm.

Figure 5.4: Fat-intensity curves of the 970 nm and 1300 nm LED test. The result of each replicate measurement is represented by the blue dots. The pink line represents the result of the linear regression, performed on the data between 0% and 60% fat.

As displayed in the graphs, for both wavelengths there was an approximately linear behavior up to 60% fat. Although a general linear trend was visible, the replicate measurements for each phantom were spread across a wide intensity range, and the distribution around the mean was relatively homogeneous. The 82% and 100% samples led to much smaller scaled intensities. Thus, the last two groups for each wavelength were not included in the linear regression.

The result of the linear fit performed on the mean value of each group of replicates is displayed by the pink line in Fig. 5.4. The fat-intensity relationship at 970 nm was described by $y = 0.04454x + 0.84$, with an R^2 value of 0.83. High residuals could be observed at the 30% point, where the mean intensity was higher than the expected value.

For the 1300 nm LED, the linear regression estimated the following function $y = 0.035x + 0.1616$, with an R^2 value of 0.80. A clear outlier was visible at 32%, where most replicates fell higher than the fitted line. For both wavelengths, the goodness of fit was acceptable, but the estimated function was different from the one found during the proof-of-concept test, presented in Section 4.4.

5.3.3. DRS vs. LED-test

The outliers at 32%, 82% and 100% were partially reflected (inverted) in the scaled DRS spectra in Fig. 5.2. Here, scaled values at 970 and 1300 nm consistently increased with fat percentage, with the exception of 81% and 100%. At 1300 nm, the scaled intensity of the 32% phantom was slightly higher than that of the 40% phantom, similar to the results of the LED test in Fig. 5.4. These results were compared to the shape of the estimated scattering and absorption, although only information above 1000 nm was available. The slope of the spectra between 1200 nm and 1300 nm was calculated as the difference in mean values (μ): $\mu_{1200} - \mu_{1300}/100$ to represent the differences in the reduced scattering and absorption between the two wavelengths. Fig. 5.5 displays the slope values plotted against the fat content. As the slope is always negative, a smaller value means a bigger reduction in the coefficient from 1200 nm to 1300 nm. With the exception of the 0% spectra, the slope and thus the absorption coefficient decreased with fat between 1200 nm and 1300 nm. Contrarily, the scattering slope of the 82% and 100%-fat samples were flatter than the rest (lower absolute value), interrupting the semi-linear trend. Looking at the 32% phantom results, the slope of the absorption spectrum between 1200 and 1300 nm was steeper than the adjacent points.

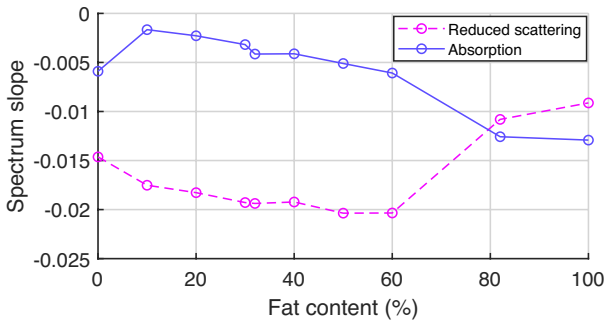

Figure 5.5: Slope of the reduced scattering and absorption profiles, calculated between 1200 and 1300 nm. The slope is calculated as $\mu_{1200} - \mu_{1300}/100$ for each fat percentage. As the slope is always negative, a smaller value means a bigger variation between the coefficient at 1200 nm and 1300 nm.

The gradient at 970 nm was not well defined in the scaled DRS spectra, so no direct correlation could be identified with the scaled intensity values at 30%. The reduced scattering and absorption were not available at that wavelength, so no comparison was possible in that range.

5.3.4. LED-test comparison

Due to the large variability of the samples, further analysis was conducted to investigate its source. To start, the scaled intensities of the two tests (t2 and t3), performed in consecutive days, were separated and plotted with the scaled intensities measured during the proof-of-concept test (t1). The results for LED 970 nm and 1300 nm are depicted in Fig. 5.6. From the plots, we could immediately distinguish the difference from the proof-of-concept test, already highlighted with the linear regression. Aside from this, an important effect was the clear offset between measurements conducted during the first and second day of the validation test. The 970 nm plot displays an average negative offset of -0.41 ± 0.1748 between t2 and t3; while for the second wavelength there was a positive variation between t2 and t3, with an average difference between the means of 0.1494 ± 0.0351. Aside from this difference, which mainly reflected in the y-intercept when assuming a linear relationship, the results were relatively consistent: taking into account the different number of samples (4 for t2, 6 for t3), the variability between replicates was similar, and the outliers found in Fig. 5.4 were visible for both t2 and t3. The reasons and implications of these findings are explored further in the discussion.

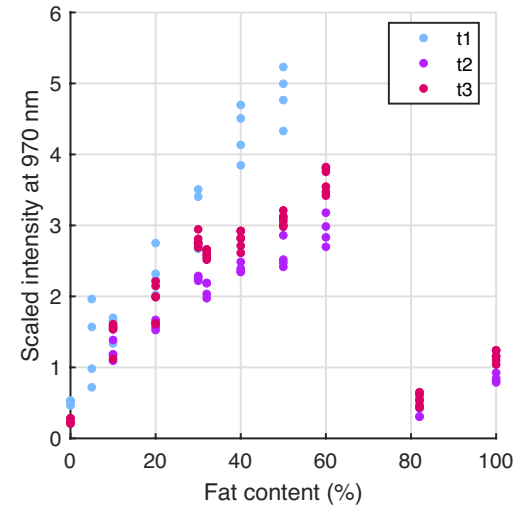

a) Fat-intensity plots at 970 nm

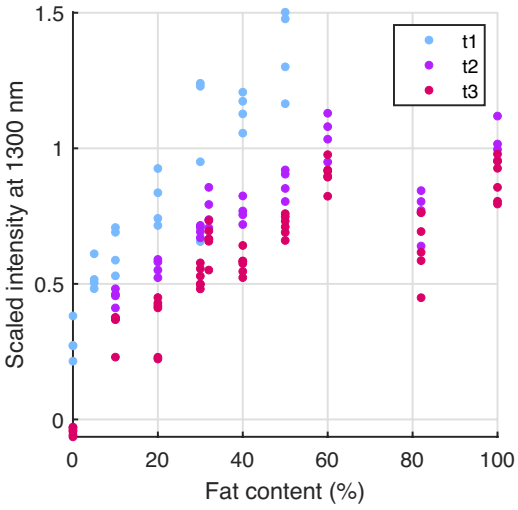

b) Fat-intensity plots at 1300 nm

Figure 5.6: Comparison of the scaled intensities measured for the three LED-tests, plotted against the corresponding fat percentage. t1 is associated with the proof-of-concept test, while t2 and t3 are the results of the validation test recorded during the first and second day, respectively. a) reports the results at 970nm, while b) at 1300 nm.

5.4. Discussion

5.4.1. DRS measurements

Overall, the DRS reflectance spectra, absorption, and reduced scattering of the new phantoms did not show significant differences with the previous experiment. The scattering amplitude was slightly more consistent between different phantoms. However, the f/w-ratio estimation by the DRS machine was inaccurate. Possible causes may have been the small SDS, for which the Farrel model loses accuracy, calibration of the needle probe, or the addition of TG which may have altered the optical properties. Inaccuracies in the fabrication process or storage of the phantoms could have caused small variations from the expected lipid content, but do not explain such a large offset. Regarding the 82% sample, the fat content was known, as the phantom corresponded to the store-bought butter, but the overestimation by the estimation model highlights a possible limitation of DRS, which could be reflected in a multi-wavelength system. The overall effect of these variations between expected and effective f/w-ratio needs to be carefully evaluated in relation to the LED-test results.

5.4.2. Fat-intensity relationship

The primary goal for the validation test, represented by the first research sub-question, was to confirm the existence of a linear relationship between the measured intensity at 970 nm and 1300 nm, after scaling at 1200 nm, and the lipid content of the sample. An evident linearity was observed between 10% and 60% fat (and, to an extent, 0%, although fewer samples were available). However, the off-the-counter 82% and 100% phantoms resulted in significantly lower values, and a larger deviation from the line was observed at 30% for the 970 nm curve, and at 32% in the 1300 nm curve.

From comparison with the scaled DRS spectra and estimated optical parameters, the behavior of the 32%, 82% and 100% phantoms could be traced back to the change in scattering or absorption between different wavelengths. Specifically, the 32% outlier corresponded to a slight deviation in the slope of the absorption coefficient from the semi-linear behavior. More interestingly, the 82% and 100% behavior in the LED-test could be associated with variations in the scattering profile, explained as follows: for those phantoms, the absorption slope was steeper than for lower fat percentages. A steeper slope means a higher reduction in absorbance and thus reduced light loss in the tissue. This should have resulted in higher scaled intensity in the LED-test. However, the scattering slope was much lower for these two phantoms than for the rest. As the scattering did not decrease significantly between 1200 nm and 1300 nm, light was dispersed in the tissue in a similar way, resulting in the low scaled-intensity values that were noticed in 4.10.

The scattering behavior of the margarine and butter sample was expected to differ from the rest, as per experimental design. On the other hand, the same lard material used in the 100% phantom was

also used for the gelatin samples, and is expected to represent human lipid tissue properties. Thus, while the deviation of the butter and margarine phantoms from the linear behavior is not necessarily a limitation for clinical applications, the low values detected for the 100% swine lard sample should be further investigated. Overall, these results highlight the dependence of the fat-intensity curve on the scattering properties of the probed material, answering the third research sub-question.

The outlier at 32% was explained by the composition of the phantoms, but the one at 30% in the 970 nm fat-intensity curve could not be explained by comparison with the DRS measurements. This variation can be attributed to imperfections in the custom-made phantom holder, given that the same variation was visible in both t2 and t3. Another possible explanation is that the effective fat fraction was higher than expected, although the estimated fat percentage with the Farrel model was 21.71% (SD 0.73).

5.4.3. Inter and Intra-test variability

Even excluding the high-fat phantoms, the linear functions at both 970 nm and 1300 nm did not correspond to those found in the previous study, in terms of slope and y-intercept parameters. Furthermore, the validation test was carried out over two days to increase the sample size, under the assumption that the testing conditions would be the same. However, the comparison between the results obtained in two consecutive days showed a clear difference, reflected mainly in the y-intercept of the linear function. In relation to the second sub-research question, these results showed that, although a linear relationship may be present between fat content and scaled intensity, its parameters are not well defined and vary depending on the experimental conditions.

Differences between the tests could have been caused by many factors, either directly associated with the measured optical properties or external. Specifically, the offset between t2 and t3 appeared relatively systematic between fat percentages. It was also observed in both wavelengths, albeit negative in one case, and positive in the other. The test was performed across two days, meaning that the LEDs were repositioned, possibly leading to a slight variation of SDS or orientation of the light source. On the other hand, the phantoms were repeatedly refrigerated and brought back to room temperature, which may have caused water evaporation or changes in the size of the molecules [18]. DRS measurements were performed only on the second day, so they could not be used to retrieve more information on the matter.

Differences in the linear relationship from the proof-of-concept test to the validation test may have been the results of similar effects. In addition, several experimental conditions changed between t1 and t2/t3. Assuming that the reduced SDS affected all wavelengths in the same way, the main difference could be attributed to the phantoms, which were produced with a different formula.

Although only small variations in the scattering and absorption profiles were observed, their influence may have been significant. In t1, the estimated fat content of each phantom was closer to the expected value, while there was a notable offset in the results of t2. If we used the estimated fat% values to plot the fat-intensity relationship, the curve for t1 would remain relatively similar, while the curve of t2 would be steeper for both wavelengths. Nevertheless, the functions found during the first test would not be validated. Although the initial setup was improved, this test highlighted that the setup was inherently a source of variability, and thus no direct conclusions could be drawn. Nonetheless, a specific relationship was observed between the lipid content and the measured signal, regardless of the confounding factors. Although at this stage it was not possible to identify the determinants of its parameters, this study demonstrated that differences in tissues can be detected by probing only at a few relevant wavelengths, motivating further research. To build a robust optical detection method based on this concept, the relationship between optical response and tissue composition needs to be investigated in a more controlled setting. The first step in this direction is the transition to reflectance-based measurements, which offer a more stable measurement method and simultaneously offer more opportunities for practical implementation.

6. Instrumentation Tests

6. Instrumentation Tests

The tests carried out with the sensor board and the LEDs in transmittance configuration provided a proof-of-concept method for multi-wavelength tumor discrimination in breast, but the setup adopted for these tests is not suitable for clinical implementation. In Ch. 2, the results of the literature review highlighted that, for real-time tumor margin detection during BCS, the optical sensor must probe the tissue "from the outside", so a reflectance-based configuration is necessary. Furthermore, a multi-wavelength device must simultaneously probe the tissue with different wavelengths and discern the optical response of each. Optical fibers can be used to transport light and achieve an SDS of 1-4 mm. This is necessary to obtain a probing depth of 2 mm, which guarantees resections with a margin of healthy tissue around the tumor.

Multiple tests were performed to demonstrate the feasibility of integrating multi-wavelength optical measurements into a hand-held device. The main research questions were:

1. Is the optical signal detectable in reflectance-based measurements?

2. Can differences in fat concentrations be distinguished in the detected signal?

The prototype sensor board was used in combination with the needle probe previously used for the DRS measurements. Two fiber-coupled laser diodes were tested individually to investigate the signal quality achievable in this configuration. A second needle probe was then employed with the sensor board to operate the two light sources simultaneously, and to demonstrate the correct operation of the multi-wavelength measurements. Finally, the multi-wavelength device was tested with the same samples used for the LED tests to investigate its sensitivity to different tissue compositions.

In this chapter, the instrumentation used for the tests is presented. Then, the tests conducted and their results are described and interpreted in light of the research questions.

6.2. Experimental Setup

6.2.1. Laser diodes

Laser diodes were chosen as light sources because of their high injection power and precise wavelength output, which allows the specific absorption features of the chromophores to be pinpointed with more precision. Two fiber-coupled NIR laser diodes were already available from previous research, focused at 1270 nm (Shengshi Optical, China) and 1310 nm (Qphotonics, LLC, USA). As the goal of the test was demonstrating the operation of the device, and the possibility to detect a signal in reflectance configuration, the two diodes were used although the wavelengths did not comply with the findings from previous tests. According to the specification sheets, the 1270 nm laser had a 63 mA maximum operating current and was rated at an output power of 5 mW, while the 1310 nm was rated at 150 mA and 3 mW. Thus, the diodes were powered with the 46 mA and 100 mA current outputs of the board. The lasers were connected via fiber optic connectors to the needle probes.

6.2.2. Needle Probes

Two different custom-made optical needle probes (Philips Research, Eindhoven) were used. The first one (needle 1) was the same one employed for the DRS measurements. It consisted of two optical fibers (emitter and receiver), separated by a 2.1 mm SDS. With this instrument, only one laser could be connected to the probe at a time. The second probe (Probe 2) was a multi-distance needle probe, schematically described in Fig. 6.1.

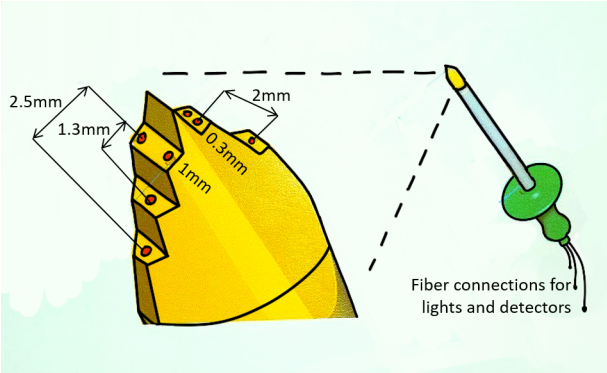

Figure 6.1: Schematic representation of the multi-distance optical needle.

It was made up of seven optical fibers, situated at different distances from each other. By selecting which fiber is connected to source and detector, the desired SDS could be selected, and multiple light sources could be employed simultaneously. The two lasers were fixed at a distance of 0.3 mm between each other, with an SDS of 2 mm from the collecting fiber. The photodetector was integrated into a custom-made optical fiber connector. For the measurements, the needle probe was fixed in a vertical position with a needle holder. The sample was placed below it on a vertical manual stage (Thorlabs, USA), which was used to precisely position it with respect to the needle tip. Fig. 6.2 represents the test setup.

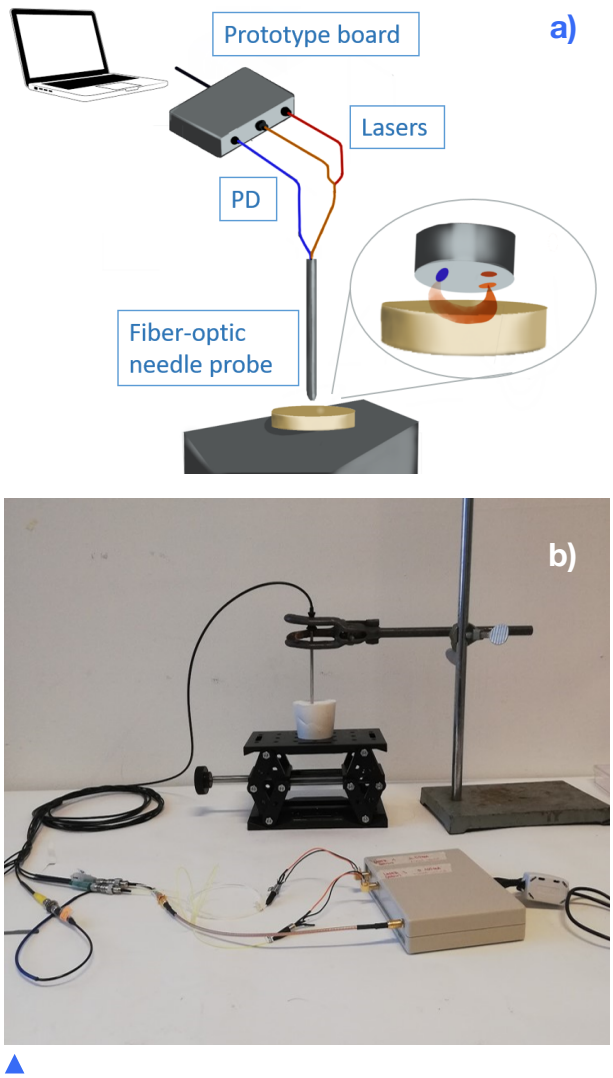

Figure 6.2: Schematic (a) and picture (b) of the test setup including the prototype board, connected to the laser diodes and photodetector (PD) via coaxial connectors. The sources and detector are connected to the optical needle via optical fibers. The needle is fixed in a vertical position over the phantom, which can be moved via a manual linear stage for insertion and replacement.

6.3. Results & Discussion

6.3.1. Laser Output Power

Depending on their power, lasers can pose a risk to the safety of the eye and skin: While only power ratings above 500 mW are considered dangerous for the skin, prolonged exposures of beams above 0.39 mW can cause permanent damage to the retina. On the other hand, high power outputs mean that more light is collected by the sensor, leading to a better SNR. As the output power of lasers depends on the operating current, and may deviate from the specifications (for example due to the optical fiber coupling), accurate tests are necessary to characterize the light sources and ensure their safety.

For both lasers, the average output power at the end of the optical fiber, for constant driving currents, was measured with two different power meters (PM100D – Compact Power and Energy Meter Console, Thorlabs, USA; EO Deluxe power meter, Edmund Optics, USA). However, the measurement setup and sensor characteristics were not suitable for the desired application, so only rough measurements were possible. The measured output power was estimated around 7-9 mW for the 1300 nm laser diode, and 8-12 mW for the 1270 nm diode. Although not fully reliable, these measurements presented larger output power compared to the expected values.

In fiber-coupled lasers the light emitted from the optical fiber diverges, so the power density of the source, defined as output power (in Watts) over the beam area (in m^2), decreases rapidly as the beam spreads [37]. When considering eye safety for exposed beams (i.e., when the probe is not inserted in the tissue), this allows to determine a distance at which the power output is low enough to be considered inherently safe. This distance, called nominal ocular hazard distance (NOHD), can be calculated as:

$$\text{NOHD} = \frac{\sqrt{\frac{4 \times P}{\pi \times MPE}} - d}{\text{div}} \qquad (6.1)$$

Where *div* is the divergence angle in radiants, *P* is the average output power of the beam and *d* is the start radius of the beam. The MPE is the maximum permissible exposure in W/m^2, which depends on the wavelength and duration of the exposure.

Most of the available documentation on the matter was only applicable to visible light. For reference, according to the European standard IEC 60825, the MPE value for visible light under an exposure duration below 0.25 seconds is 25.4 W/m^2, which corresponds to approximately 1 mW entering the pupil's diameter[1]. Considering for example a laser beam similar to those employed in the experiment, with *P=12 mW*, *div=0.26 rad*, and *d=1mm*, the obtained NOHD would be 9.05 cm. This would mean that the device is safe for use in most situations. However, the specification sheets did not contain all the relevant information for these calculations, so the safety distance could not be calculated exactly. More importantly, while with visible light the blink reflex impedes exposure for longer than 0.25 seconds, NIR light is invisible, and longer accidental exposures can happen.

Following these considerations and the impossibility to accurately evaluate the output power of the diodes, it was not possible to definitely determine the safety limits, and it was decided to use safety measures such as beam screening and laser goggles. In future research, the safety limits should be accurately determined. Dedicated equipment should be used to measure the power output of the light sources at the end of the bare fiber or probe, depending on the setup. Lower driving currents could then be used to obtain power levels below the safety threshold, making the device inherently safe.

6.3.2. Signal Quality Analysis

Probe 1 was used to independently investigate the quality of the reflectance output from the two lasers. A white reference tile was used to acquire a reference signal to analyze the noise, stability, and amplitude of the sensor output. Current control without PWM and with a PWM 10% duty-cycle were tested for both lasers. The sensor board measurement cycle was the same described in Section 3.2, but the raw signal was acquired before averaging in each post-integration hold period, so no offset compensation was performed. The hold, reset, and integration periods were set at 100 ms, to avoid overheating the lasers, especially without PWM. The sampling frequency was 1KHz, leading to 100 samples for each measurement cycle. An integration time of 300 ms, corresponding to a gain of $3x10^6$, proved sufficient. Each measurement lasted for 30 seconds. Fig. 6.3 shows the plot of the raw signals for both lasers.

Test measurements were also carried out with the 60% phantom by inserting the needle tip a couple of millimeters into the sample, to test if a signal

[1]The formula for the NOHD and the MPE values were obtained during a laser safety course organized by the 3mE faculty.

could be detected after light interaction with other materials. Direct laser control without PWM and a *Tint* of 100ms were employed.

The output of the 1270 nm was higher, as expected, due to the higher power current and ratings. Without PWM, values of 284.2 mV ± 2.1 were recorded for the 1270 nm, leading to a 26.77 dB SNR, against the 127.1 mV ± 0.6 at 1300 nm, with an SNR of 23.8 dB. Using a 10% duty cycle, the voltage output was much lower, reaching only 26.5 mV ± 0.6 (SNR 14.5 dB), and 10 mV ± 0.7 (SNR 4.89 dB).

The electrical noise present during the hold periods was consistent with the findings reported in Section 3.3. However, in contrast to the previously measured LED output, a source of variability was noticeable between hold periods, especially in the 1270 nm response with no PWM. The overall SNR of the signals showed that this variation was still acceptable for large voltage values, where the SNR was above 20dB, but that the latter degraded rapidly as the signal decreased.

The noise during the hold periods was purely electrical, as the sensor was not connected. However, these low-frequency variations were likely due to the influence of other factors. Possible causes may have been the instability of the lasers due to temperature build-up, power supply instabilities, or, in the case of PWM, pulse-to-pulse instability. The relatively high source current may have also been relevant.

In this setup, passive cooling of the lasers was allowed by setting longer hold and reset periods, during which the laser was off. In general, PWM control can improve thermal stability by turning on the diodes for only 10% of time, at a very high frequency. On the other hand, it can be an additional source of noise and decreases the average output power by a factor of 10, according to the duty cycle.

For the measurement with the 60% phantom, a mean of 18.4 ± 0.6 mV (in a 0-1200 mV range) was detected with the 1270 nm laser, while the 1310 led to a mean output of 5.7 ± 0.8 mV. The 60% fat phantoms were chosen as high fat percentages lead to bigger light losses, so a “worst conditions” test was performed. Nevertheless, it was possible to measure the reflectance signal. A small *Tint* of only 100 ms was selected, so a simple way to improve the SNR in the future could be increasing

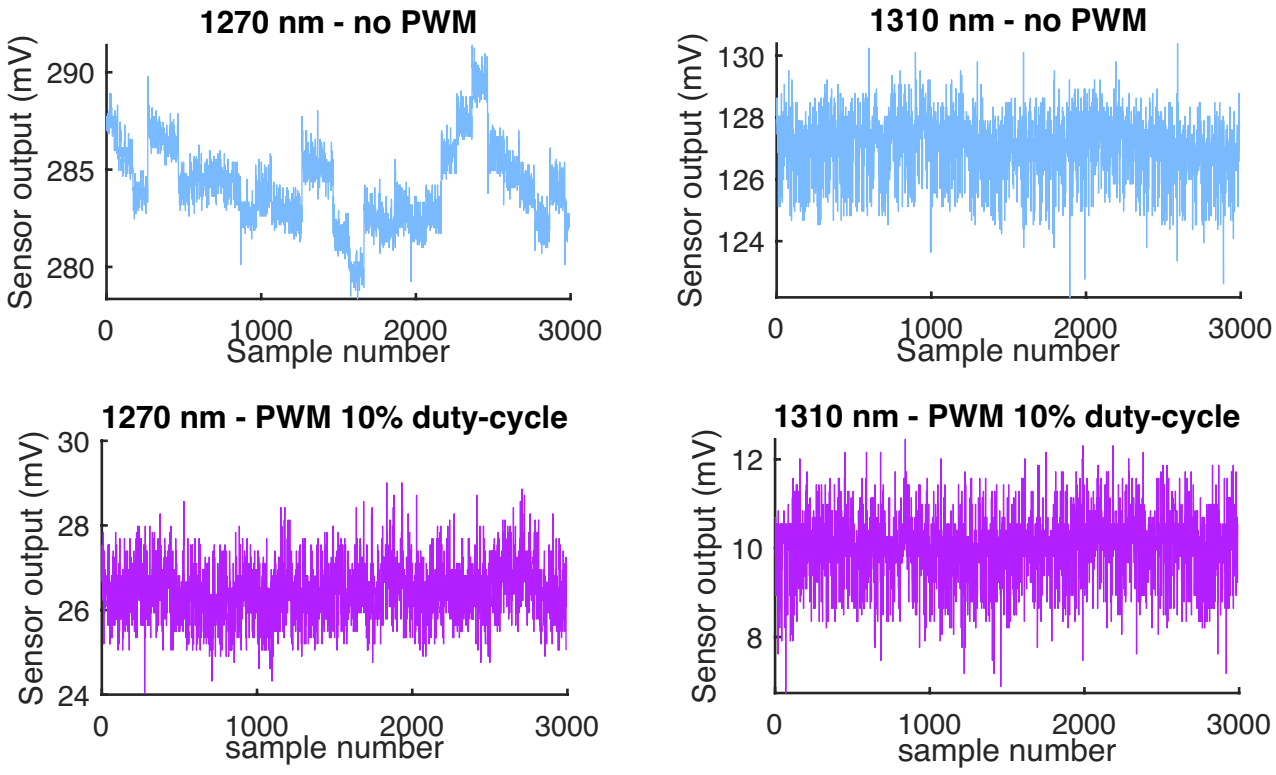

Figure 6.3: Plot of the raw sensor data acquired by the device, before averaging, measured with a white reference tile. On the left, the intensity of the 1270 nm laser with constant current source and PWM 10% duty cycle. On the right, the detected intensities with the 1310 nm laser.

the integration time to have a bigger gain. Although further investigation into the sources of noise and instability of the signals are necessary, this test demonstrated that it was indeed possible to detect a signal with the current setup. Furthermore, the test with the 60%-fat phantom showed that laser-based reflectance measurements with the optical fiber needle were possible, answering the first research sub-question.

6.3.3. Multi-wavelength measurements

Probe 2 was used to demonstrate the multi-wavelength device operation by probing a number of tissue-mimicking samples with different fat percentages. As explained in Section 3.2.2, the lasers were turned on alternatively for the duration of *Tint,* and the average values of the two post-hold integration periods (corresponding to the response of the two wavelengths) were transmitted simultaneously at the end of each measurement cycle.

Preliminary tests showed a much higher intensity loss with the second probe, so higher integration times were used to compensate, along with a constant current source. A *Tint* of 5000 ms was necessary to detect a signal after light interaction with the samples, while the hold and reset times were kept at 100 ms, leading to a total measurement cycle of 10.6 seconds. Each measurement was acquired for about 30 seconds to obtain three samples. First, three reference measurements were taken to calibrate the system by placing the white reflectance tile 5 mm below the needle tip. Then, the test was carried out with the same samples used for the second LED-test, described in Ch. 5 (0%, 10%, 20%, 30%, 40%, 50%, 60%-fat custom-made gelatin phantoms, 32%-fat margarine, 82%-fat butter and 100% swine lard). For each phantom, three measurements were taken at three locations by inserting the tip of the needle into the sample. The test resulted in a total of 99 samples for each wavelength. Fig. 6.4 shows the results of the test.

Fig. 6.4a reports the average intensities at the two wavelengths after calibration (normalization based on the average reference signal). The 82% butter sample led to highly variable measurements. This was probably due to the consistency of the sample, which, regardless of the time spent at room temperature, had a hard consistency. This may have led to the disruption of the sample's structure during needle insertion.

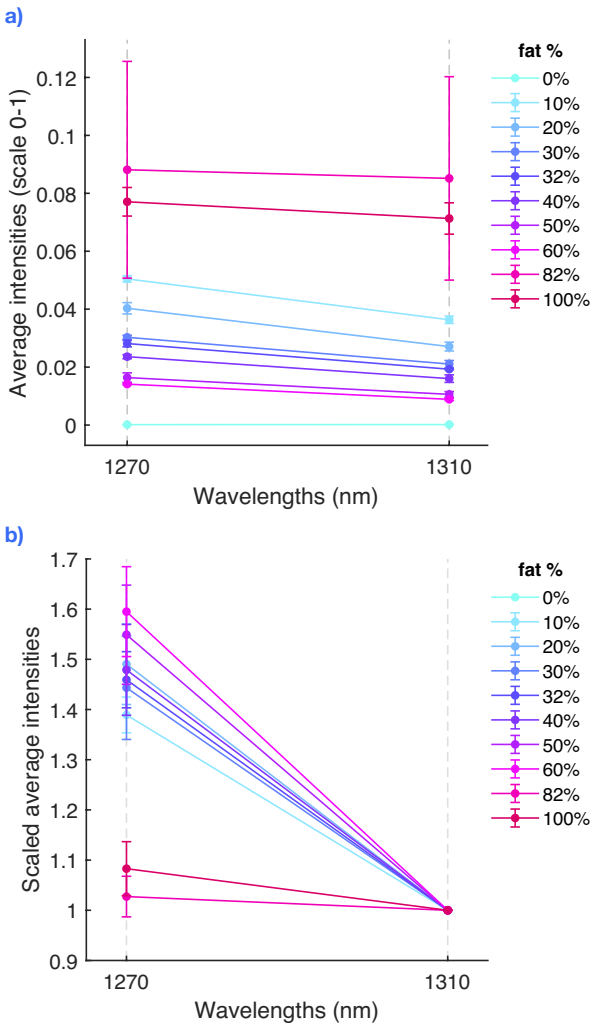

Figure 6.4: Plot of the average intensity values (± SD) after calibration (a), and scaled (± SD) at 1310 nm (b) to compare the spectra of different phantoms measured at two wavelengths with the multi-wavelength needle probe.

The main effect visible in the graph was that the reduction of the signal at higher fat percentages was consistent with the results of the LED test, with the exception of the off-the- shelf butter and lard. The standard deviation of the measurements was low enough to clearly discern between the outputs of the different phantoms. Unlike transmission measurement, the 0% sample led to signal intensities close to zero, due to the low scattering.

Fig. 6.4b displays the intensity values scaled at 1310 nm, to compare between the two lasers. Relatively low differences in slope were noticed between the phantoms, with no exact trend. This was expected, as the lasers were not selected based on their discrimination capability. Furthermore, the lasers output wavelengths fell into a generally low-populated absorption range,

where even in the wide-range reflectance spectrum there is not any recognizable difference between the two wavelengths. Overall, the second research sub-question was also answered, demonstrating that differences in the detected signal at multiple wavelengths, from different phantoms, were discernible with this setup.

6.4. Conclusions

The overall results of the tests showed that it was possible to probe tissue-mimicking phantoms in reflectance mode with a laser-coupled needle probe. Furthermore, differences (or similarities) between the spectral response of two wavelengths could be measured with the multi-wavelength setup.

Limitations of the first probe were mainly related to signal instability, which needs further investigation. The low voltage output with probe 2 was likely due to the needle's specifications, in terms of optical fiber type, size, or fiber coupling. For this reason, a large

T int was used, which resulted in a low sampling frequency not suitable for clinical implementation. Regardless of the low sensed voltage values, it was still possible to discern the effect of different phantom compositions. In the future, similar or higher gain levels could be achieved by using a different needle, such as the first probe, or by lowering the value of the internal capacitor of the TIA, to increase the gain at lower integration times. Once accurate temperature control is implemented to stabilize the laser's output, and noise is reduced at a hardware level, a lower hold and reset time in the order of 100 microseconds can be used to further increase the speed of each measurement cycle without losing accuracy.

The reflectance-based configuration addressed some major limitations of the LED-test setup. Specifically, the measured signal did not depend on the sample thickness anymore. This reduced confounding effects and simultaneously provided a measurement system that can be applied more easily to different types of tissue samples and phantoms. In addition, simultaneously probing two wavelengths removed variable factors that were present when measuring with two LEDs at different times. For example, the phantom's temperature and the section of sample that was probed were exactly the same for both lasers. This made the comparison between signals from the two wavelengths more accurate. On the downside, as seen in the test, reflectance-based measurements were generally characterized by lower signal amplitudes, which is consistent with the literature [38]. To achieve a better SNR, the laser output power at the end of the needle probe should be optimized to increase the signal while ensuring levels below the eye safety threshold. Another possible limitation of this setup is the probing depth. Although the SDS is constant and well defined, the probing depth of the light depends on the wavelength, so it might differ between the two light sources [39]. In the test, homogeneous tissue-mimicking samples were used, so differences in probing depth did not significantly impact the result, but this aspect should be further investigated when non homogeneous tissues are interrogated.

7.

Discussion & Future Recommendations

7. Discussion & Future Recommendations

In the previous chapters, the experiments conducted throughout this thesis project were described in detail. The results of the experiments were interpreted in relation to the research sub-questions and existing literature. Their limitations and implications for future developments were discussed in the context of the single experiment. Here, the results of the whole project are evaluated together in a higher-level analysis, which aims to answer the main research question and insert this project in the context of existing research and clinical implementation. The chapter is enriched with some practical recommendations for future work.

7.1. Working Principle

The f/w-ratio

The fat/water ratio was chosen as the most promising tissue discriminator to develop the working principle. Although this approach might seem more complex conceptually, it is favorable when direct studies on human tissue are not possible. It allows us to isolate a few significant tissue properties and devise a test protocol based on those, simplifying the process. The results of such analysis can then be generalized to other contexts where the fat and water content is a parameter of interest. On the flip side, the tests demonstrated that it was not possible to completely isolate these two properties from other characteristics of the phantoms, suggesting that a thorough analysis of all the factors that impact optical tissue measurements should precede further studies. Furthermore, throughout the study, the fat percentage was used instead of the f/w-ratio, under the assumption that fat and water were the only constituents (and absorbers) in the phantoms. The implications of this assumption should be evaluated before transitioning towards more complex experimental conditions.

Experimental Conditions

The choice of transmittance-based measurements with LEDs to investigate the working principle was ruled by technical limitations and time constraints. Initially, these were not considered detrimental factors, although the setup did not fully represent the actual conditions of future clinical applications. Differences in the transmission spectra between wavelengths could be detected, proving that the choice of light source was suitable for the tests. The difference in results between the two different 1300 nm LEDs highlighted that the choice of component may have an influence on the results. Nonetheless, when considering the 1300L LED, similarities with the phantom measurements with DRS and lasers suggested that the results of the working principle analysis are transferable to other setups. On the other hand, the transmittance-based configuration turned out to be the main limitation of the experiment, due to the high dependency of the measurements on the distance between light source and sensor.

The fat-intensity relationship

Despite the variability in the measurements, it was still possible to perform the tests. The light intensity measured at each wavelength was scaled at 1200 nm, obtaining the ”scaled intensity”, which actually represented the ratio between the light intensity measured at the respective wavelength and at 1200 nm. A linear relationship was found between the fat percentage of the phantoms and the scaled intensity at both 970 nm and 1300 nm. Through the validation test, it was found that the parameters of these linear relationships did not depend only on the absorption of lipid and water, so it was not possible to define a direct method to convert intensity measurements into f/w-ratio values. However, the results of this test are promising, as they offer a proof-of-concept of a simple detection method. A similar working principle is used in one of the most common devices for physiological monitoring: the pulse oximeter. This device can estimate the blood oxygen saturation from optical measurements using a very simple and effective system: the difference in absorption between two chromophores (oxyhemoglobin and reduced hemoglobin) is reflected in the ratio of transmitted light through tissue at a red and infrared wavelengths and used to measure relative changes in the total hemoglobin concentration. An empirical curve is then used to relate this ratio to the blood oxygen saturation of the sample [40]. Similarly, in the system proposed in this project, the scaled intensity at a certain wavelength actually consists in the ratio between the intensity at that wavelength, and at the reference wavelength. Once the linear fat-intensity relationship is well defined, it can be used as a calibration curve to infer the fat/water ratio of the tissue.

Implications of the results

The factors affecting the parameters of the fat-intensity curve were not clear. However, some conclusions could be drawn from the results:

- Comparing the tissue response between a few relevant wavelengths contains information on the tissue composition. This method is potentially more robust than comparing the absolute intensities obtained from different types of phantoms or tissue.
- Scattering influenced the fat-intensity relationship. Although in this context this resulted in a confounding factor, the effect of scattering may be exploited to generate discrimination models for multi-wavelengths measurements.

Empirical vs Computational approach

This study adopted an empirical approach, which was hindered by the inherent limitations of the setup, and by the choice of phantoms which did not perfectly simulate optical tissue properties. To progress with this perspective, the findings

should be validated with improved setup and tissue phantoms, to understand the exact factors that influence its parameters. Examples of a similar approach were found in the studies by Keller et al. [41] and Bogolomov et al. [21]. Contrarily, a computational approach based on the DRS and a-priori knowledge could be used, similarly to the method proposed for scattering compensation in Appendix D. As previously described in Ch. 4.5.4, simulations, computational models, and optimization algorithms can be employed to extract relevant relationships based on the DRS spectra, as shown in prior research studies [12, 13, 16, 26], and only tested with the multi-wavelength device as a last step.

Wavelength choice

The NIR range was chosen to better capture the absorption features of fat and water. Other studies with DRS developed chromophore-based discrimination algorithms in the visible range [10]. This light range requires simpler equipment and can account for the influence of many discriminating factors. However, the main advantage of using NIR light is that blood absorption doesn't have any influence in this range [10, 13]. This is necessary for use during surgery, where blood surrounding the instrument's tip can contaminate the measurements. Furthermore, NIR and IR photodetectors are less affected by ambient light interference and show bigger differences in reflectance spectrum from healthy to tumorous tissue in breast [10, 28]. Higher wavelengths, however, proved unsuitable for this application, as the high water absorption above 1400 nm hindered light transmission and signal detection.

7.2. Instrumentation

Sensor performance

Throughout this research project, the multi-wavelength prototype sensor was optimized. The sensor was able to detect a wide range of signals with high precision and resolution. However, for signals below 30 mV, a system based on the programmable gain of the transimpedance amplifier had to be used to improve the SNR. Overall, no significant offset was noticed, and noise levels were considered suitable for the application. However, all the measurements were static, meaning that the signal was expected to be constant over time. In real applications, the movement of instrument or probed tissue might hinder signal detection. Furthermore, smaller differences in tissue content might need to be discriminated, requiring a high level of accuracy and precision. The exact influence and sources of noise, non linearities and offset should then be quantified via a dedicated performance analysis.

Feasibility of the reflectance-based configuration

Tests with a reflectance-based setup were performed to demonstrate the feasibility of measuring in this configuration. The tests, conducted with lasers and two ready-available needle probes, proved that the reflectance tissue response was measurable both with a single and dual wavelength system. Some limitations in terms of signal stability and acquisition speed were already addressed in Ch. 6 and seemed relatively easy to improve. The results of the dual-wavelength prototype were generally consistent with the expected values from the DRS spectra, suggesting that the measurements were accurate. However, this study was approached only in the final phase of the thesis, so, because of a lack of time, only the readily available wavelengths were tested, which were not deemed relevant for chromophore identification.

Lasers as light sources

The results of the test showed that lasers are a potential good fit for future implementation of the device. Compared to LEDs, their highly focused wavelength output (usually ± 3 nm around the output wavelength, compared to the ± 50 nm in LEDs) is more suitable to detect the sharp absorption features of the chromophores, and might lead to better results for tissue discrimination. On the other hand, lasers are more expensive and may pose a hazard for eye and skin safety. When used with optical fibers, it is likely that the beam divergence is enough to render them safe upon some calibration. However, LEDs could be a cost-effective and safe alternative for the optical probe, as they require simple driving circuits, low power, and their non-collimated output is preferred in terms of eye and skin safety [42]. For these reasons, their use in future iterations should be explored further. For example, the LEDs used in this study ranged from a power output of 1.5 to 9 mW, which is relatively low for non-collimated light sources. High-power LEDs could be used instead to achieve a better signal. More suggestions regarding the choice of light source are presented as future recommendations in Section 7.4.

7.3. Limitations Towards clinical implementation

The starting point of this thesis project was DRS, which we aimed to simplify. The instrumentation and working principle of DRS heavily impacted the research approach and final embodiment of the multi-wavelength sensor. As a result, some of the limitations of DRS for clinical implementation, identified during the literature review, are also reflected in this system.

First of all the working principle was based on prior studies conducted mainly on ex-vivo tissue samples. In reality, there might be differences between the optical behavior of the latter compared to in-vivo situations where temperature, blood and water concentrations, and the influence of other absorbers may differ [13].

For further developments, the inter-patient variability and the dishomogeneity in breast morphology within the same breast may also affect the discriminating parameters between tumor and benign tissue [12, 26], requiring some correction factor or reference measurement to apply the calibration curve (fat-intensity relationship) in practice.

The penetration depth at different wavelength may also pose a limitation: while in reflectance configuration the SDS is constant, in fact, the light path is not well defined, so two wavelengths may probe different layers of tissue [28, 39].

Concerning the instrumentation and ”hardware” side, limitations can be identified both looking at DRS and at existing LED-based device for chromophore discrimination. The experiments conducted in this study were static, but in clinical applications motion artifacts may significantly hinder the signal acquisition [43]. Optical shunt (direct light transmission from source to detector, without passing through the tissue), may also cause inaccuracies if the probe is not fully inserted in the tissue [40]. Furthermore, due to possible power variations and light source conditions, recurrent user calibration is required. The current calibration method is performed with a specific (and expensive) reflective tile, which is not ideal for implementation.

Some of these limitations concern the final mechanical design of the device, which was addressed in the thesis of P. Callaert. Others should be considered when developing the working principle and circuit/software design. Suggestions on this regard are presented in the following section.

7.4. Future Recommendations

Although the results are promising, this thesis represents only the very first step towards the development of a multi-wavelength device for IMA in breast.

The working principle and instrumentation were separated in two research lines, and investigated independently. The proposed working principle was not robust, so further investigations should be carried out to propose a better alternative based on tissue modeling and DRS data. Then, the next step is to combine the two aspects: the working principle of the optical measurement can be implemented in a reflectance-based configuration with the appropriate probing wavelengths, to test and to hopefully validate a novel tumor margin detection method.

This step could be performed with the same reflectance-based setup and instruments used in Ch. 6, by simply replacing the lasers. However, to improve the reliability of the measurements and thus the significance of the results, the sensor’s performance should be improved. For example, electrical noise can be reduced with analog signal processing, timing inaccuracies can be improved by including an analog clock circuit, and the overall resolution can be increased with an external ADC. Finally, effective temperature control of the light sources can be implemented to obtain a stable output.

After the working principle is validated, efforts should focus on transforming the system into a device suitable for clinical practice. In the experiments, a custom-made needle probe was used, attached to the sensor board via optical fibers. To integrate the system in the surgical workflow, the sensor should be miniaturized and integrated in a single, hand-held surgical instrument.

The first and most important consideration on this matter is the choice of light source and detectors. Although lasers proved to be a viable option, in fact, there might be alternatives more suitable for the desired application. For example, pulse oximeters use a multitude of bare LEDs and photodiodes for reflectance measurements [24, 25, 42, 44]. Usually, the size of these devices is too

large for integration in the tip of a surgical probe, but advances in microfabrication are now allowing to build LEDs in sub-millimeter size, such as the ones used in implants for optogenetics [45]. With some optimization in terms of power and fiber-coupling, coupling LEDs with optical fibers [21] could also be a viable option. As an alternative, in literature there are also examples of the use of broadband light sources in combination with off-the-shelf spectrometers in a size of 2-10 cm, [46, 47], or chip-sized spectrometer consisting of an array of narrow band photodetectors [48]. With these solutions, the working principle could be based on continuous spectra analysis instead of multi-wavelength measurements, so the principles of DRS would be more easily transferred. Overall, each possible solution comes with pros and cons. The tradeoff between cost, size and performance needs to be evaluated depending on the chosen application, keeping in mind that changing the chosen light source (e.g. from LED to laser) at different stages of the device's development may also be beneficial.

Once the sensor and light source are chosen, portability of the system and miniaturization of the electronics should be addressed. The first aspect mainly concerns powering the device with batteries and disconnecting it from the computer through on-device data processing and storage. Coding of the microprocessor can be done to implement real-time feedback to the surgeon, a dedicated calibration sequence, and background light compensation. Concerning the second aspect, surface mounted components and suitable circuit design should be sufficient to highly reduce the size of the device. A dedicated microcontroller can also replace the Teensy, which is currently the largest component of the circuit.

To address some of the limitations mentioned previously, different SDS could be selected for each wavelength, based on the penetration depth of each. Multiple sources of the same wavelength can also be used to probe in different directions, and make the system more robust to movement of the probe. Motion and temperature sensors, with feedback loops, can compensate for thermal and motion artifacts [21, 49, 50]. Finally, an additional visible light source can be integrated to ensure eye safety by making the light visible to the surgeon, and indicate whether the light is on.

Once a working multi-wavelength device is obtained, it can be used to easily test different wavelengths, configurations and transformations of the measured output to further test and study the tissue discrimination method. The portable design can simplify experiments with different types of tissue in-vivo and ex-vivo, to promote further research towards an effective intraoperative margin assessment device. The same principles and instrumentation can also be investigated for the detection of other types of tumors.

8.
Conclusions

8. Conclusions

Throughout this thesis project, the possibility to detect breast tumor margins with multi-wavelength optical measurements was investigated.

The main research question, “can we use multi-wavelength optical measurements for real-time discrimination of tumor tissue during BCS?”, was explored under two aspects: the optical discrimination method used to differentiate between tissues, and the physical requirements and aspects of a device able to do this.

The working principle was explored through two experiments, conducted with a transmittance-based setup using a number of LEDs and phantoms. The f/w-ratio was chosen as indicator of the tissue type (malignant or benign), and a proof-of-concept method was determined from the first test, based on the apparent linear relationship between the lipid content of the phantoms and the ratio of measured intensity output at different wavelengths. With the second test, the presence of a linear relationship was corroborated. However, it was found that this relationship was highly influenced by scattering of the tissue, and would thus vary depending on the chosen phantom, making it impossible to use it for direct conversion of the sensor’s output into information on the tissue type.

The instrumentation was explored with a number of tests using a reflectance-based needle probe and laser light sources. Despite some limitations in terms of noise and instability of the signal, the tests demonstrated the possibility to measure the optical response of phantoms in this configuration. Although the setup used was not yet suitable for integration in a hand-held device, it illustrated the feasibility of achieving such system.

Overall, the results highlighted that although it is possible to build a multi-wavelength system able to measure the optical tissue response in an intraoperative setting, the working principle of the device still requires investigation. As a result, a definite answer to the research question cannot be given yet, but this study certainly highlights promising results in this direction.

In light of these results, research on DRS and multi-wavelength IMA systems can be carried out in parallel. The former is still an invaluable source to generate knowledge on optical tissue discrimination, and develop effective discrimination methods. The latter, on the other hand, can focus on simple instrumentation to streamline the testing process and finally design a simple, inexpensive and portable device to improve breast cancer treatment worldwide.

References

1. Breast Cancer https://www.who.int/news-room/fact-sheets/detail/breast-cancer.

2. 'Cancer Today - The Netherlands' https://gco.iarc.fr/today/data/factsheets/populations/528-the-netherlands-fact-sheets.pdf.

3. Breast Cancer in the Netherlands, RIVM' https://www.rivm.nl/en/breast-cancer-screening-programme/breast-cancer-in-netherlands.

4. 'Breast Cancer Treatment | Iknl' https://iknl.nl/kankersoorten/borstkanker/registratie/behandeling.

5. Scimone, M. T. et al. Assessment of Breast Cancer Surgical Margins with Multimodal Optical Microscopy: A Feasibility Clinical Study. PLoS ONE 16, e0245334. ISSN: 1932-6203 (Feb. 2021).

6. Sachańbiński, T. & Radecka, B. A Review of Methods of Intraoperative Margin Assessment in Breast Conserving Surgery. Nowotwory. Journal of Oncology 71, 225–231. ISSN: 2300-2115 (2021).

7. Koopmansch et al. Intraoperative Evaluation of Resection Margins in Breast-Conserving Surgery for In Situ and Invasive Breast Carcinoma. Breast Cancer : Basic and Clinical Research 15, 1178223421993459. ISSN: 1178-2234 (Mar. 2021).

8. Fleming, F. et al. Intraoperative Margin Assessment and Re-Excision Rate in Breast Conserving Surgery. European Journal of Surgical Oncology (EJSO) 30, 233–237. ISSN: 07487983 (Apr. 2004).

9. St John, E. R. et al. Diagnostic Accuracy of Intraoperative Techniques for Margin Assessment in Breast Cancer Surgery: A Meta-analysis. Annals of Surgery 265, 300–310. ISSN: 0003-4932 (Feb. 2017).

10. de Boer, L. L. et al. Fat/Water Ratios Measured with Diffuse Reflectance Spectroscopy to Detect Breast Tumor Boundaries. Breast Cancer Research and Treatment 152, 509–518. ISSN: 1573-7217 (Aug. 2015).

11. Nachabé, R., Hendriks, B. H. W., van der Voort, M., Desjardins, A. E. & Sterenborg, H. J. C. M. Estimation of Biological Chromophores Using Diffuse Optical Spectroscopy: Benefit of Extending the UV-VIS Wavelength Range to Include 1000 to 1600 Nm. Biomedical Optics Express 1, 1432–1442. ISSN: 2156-7085 (Nov. 2010).

12. Nachabe, R. et al. Diagnosis of Breast Cancer Using Diffuse Optical Spectroscopy from 500 to 1600 Nm: Comparison of Classification Methods. Journal of Biomedical Optics 16, 087010. ISSN: 1083-3668, 1560-2281 (Aug. 2011).

13. Bydlon, T. M., Nachabé, R., Ramanujam, N., Sterenborg, H. J. C. M. & Hendriks, B. H. W. Chromophore Based Analyses of Steady-State Diffuse Reflectance Spectroscopy: Current Status and Perspectives for Clinical Adoption. Journal of Biophotonics 8, 9–24. ISSN: 1864-0648 (Jan. 2015).

14. de Boer, L. L. et al. Towards the Use of Diffuse Reflectance Spectroscopy for Real-Time in Vivo Detection of Breast Cancer during Surgery. Journal of Translational Medicine 16, 367. ISSN: 1479-5876 (Dec. 2018).

15. Wilhelmus, B. H., Jan, J., Horikx, L. & Nachabe, R. United States Patent Application Publication - Determination of a Lipid Water Ratio, 16 (Jan. 2013).

16. Lam, J. H., Tu, K. J. & Kim, S. Narrowband Diffuse Reflectance Spectroscopy in the 900-1000 Nm Wavelength Region to Quantify Water and Lipid Content of Turbid Media. Biomedical Optics Express 12, 3091–3102. ISSN: 2156-7085 (June 2021).

17. Amiri, S. A., Van Gent, C. M., Dankelman, J. & Hendriks, B. H. W. Intraoperative Tumor Margin Assessment Using Diffuse Reflectance Spectroscopy: The Effect of Electrosurgery on Tissue Discrimination Using Ex Vivo Animal Tissue Models. Biomedical Optics Express 11, 2402–2415. ISSN: 2156-7085 (Apr. 2020).

18. Amiri, S. A. et al. Tissue-Mimicking Phantom Materials with Tunable Optical Properties Suitable for Assessment of Diffuse Reflectance Spectroscopy during Electrosurgery. Biomedical Optics Express 13, 2616–2643. ISSN: 2156-7085 (May 2022).

19. Adank, M., Fleischer, J., Dankelman, J. & Hendriks, B. Real-Time Oncological Guidance Using Diffuse Reflectance Spectroscopy in Electrosurgery: The Effect of Coagulation on Tissue Discrimination. Journal of Biomedical Optics 23. ISSN: 1083-3668 (2018).

20. Nachabe, R. et al. Estimation of Lipid and Water Concentrations in Scattering Media with Diffuse Optical Spectroscopy from 900 to 1600 Nm. Journal of Biomedical Optics 15, 037015. ISSN: 1083-3668, 1560-2281 (May 2010).

21. Bogomolov, A. et al. LED-based near Infrared Sensor for Cancer Diagnostics in SPIE BiOS (ed Coté, G. L.) (San Francisco, California, United States, Mar. 2016), 971510.

22. Kamal, A. M. & Pal, U. M. Towards the Development of an Intraoperative Probe for Breast Cancer Margin Assessment. Biomedical Optics, 2 (2022).

23. el-Beshbishi, S. N., Shattuck, K. E., Mohammad, A. A. & Petersen, J. R. Hyperbilirubinemia and Transcutaneous Bilirubinometry. Clinical Chemistry 55, 1280–1287. ISSN: 1530-8561 (July 2009).

24. Teng, F. et al. Wearable Near-Infrared Optical Probe for Continuous Monitoring during Breast Cancer Neoadjuvant Chemotherapy Infusions. Journal of Biomedical Optics 22, 014001. ISSN: 1083-3668 (Jan. 2017).

25. Spink, S. S. et al. High Optode-Density Wearable Diffuse Optical Probe for Monitoring Paced Breathing Hemodynamics in Breast Tissue. Journal of Biomedical Optics 26, 062708. ISSN: 1083-3668 (June 2021).

26. de Boer, L. L. et al. Using DRS during Breast Conserving Surgery: Identifying Robust Optical Parameters and Influence of Inter-Patient Variation. Biomedical Optics Express 7, 5188–5200. ISSN: 2156-7085 (Nov. 2016).

27. Bogomolov, A. et al. Development and Testing of an LED-Based Near-Infrared Sensor for Human Kidney Tumor Diagnostics. Sensors 17, 1914. ISSN: 1424-8220 (Aug. 2017).

28. Brown, J. Q., Vishwanath, K., Palmer, G. M. & Ramanujam, N. Advances in Quantitative UV–Visible Spectroscopy for Clinical and Pre-Clinical Application in Cancer. Current Opinion in Biotechnology. Analytical Biotechnology 20, 119–131. ISSN: 0958-1669 (Feb. 2009).

29. van Berckel, P. Developing a Breast Phantom to Test and Validate the Smart Electrosurgical Knife (2020).

30. Kho, E. et al. Imaging Depth Variations in Hyperspectral Imaging: Development of a Method to Detect Tumor up to the Required Tumor-Free Margin Width. Journal of Biophotonics 12, e201900086. ISSN: 1864-0648 (2019).

31. Nelson, T. R., Cerviño, L. I., Boone, J. M. & Lindfors, K. K. Classification of Breast Computed Tomography Data. Medical Physics 35, 1078–1086. ISSN: 2473-4209 (2008).

32. Michaelsen, K. E. et al. Anthropomorphic Breast Phantoms with Physiological Water, Lipid, and Hemoglobin Content for near-Infrared Spectral Tomography. Journal of Biomedical Optics 19, 026012. ISSN: 1083-3668 (Feb. 2014).

33. Farrell, T. J., Patterson, M. S. & Wilson, B. A Diffusion Theory Model of Spatially Resolved, Steady-State Diffuse Reflectance for the Noninvasive Determination of Tissue Optical Properties in Vivo. Medical Physics 19, 879–888. ISSN: 0094-2405 (1992 Jul-Aug).

34. Evers, D. J. et al. Diffuse Reflectance Spectroscopy: Towards Clinical Application in Breast Cancer. Breast Cancer Research and Treatment 137, 155–165. ISSN: 1573-7217 (Jan. 2013).

35. Bydlon, T. M. Intra-Operative Assessment of Breast Tumor Margins Using Diffuse Reflectance Spectroscopy PhD thesis (2012).

36. Nachabé, R. Diagnosis with near Infrared Spectroscopy during Minimally Invasive Procedures PhD thesis (2012).

37. Specifications Tutorial - Laser Safety Glasses - Thorlabs https://www.thorlabs.com/new-grouppage9.cfm?objectgroup_ID=762.

38. Venema, B., Schiefer, J., Blazek, V., Blanik, N. & Leonhardt, S. Evaluating Innovative In-Ear Pulse Oximetry for Unobtrusive Cardiovascular and Pulmonary Monitoring During Sleep. IEEE Journal of Translational Engineering in Health and Medicine 1, 2700208. ISSN: 2168-2372 (Aug. 2013).

39. König, V., Huch, R. & Huch, A. Reflectance Pulse Oximetry–Principles and Obstetric Application in the Zurich System. Journal of Clinical Monitoring and Computing 14, 403–412. ISSN: 1387-1307 (Aug. 1998).

40. Sinex, J. E. Pulse Oximetry: Principles and Limitations. The American Journal of Emergency Medicine 17, 59–66. ISSN: 07356757 (Jan. 1999).

41. Keller, A., Bialecki, P., Wilhelm, T. J. & Vetter, M. K. Diffuse Reflectance Spectroscopy of Human Liver Tumor Specimens - towards a Tissue Differentiating Optical Biopsy Needle Using Light Emitting Diodes. Biomedical Optics Express 9, 1069–1081. ISSN: 2156-7085 (Mar. 2018).

42. Hemmati, N., Setarehdan, S. & Ahmadi Noubari, H. Multi-Channel Near-Infrared Spectroscopy (NIRS) System for Noninvasive Monitoring of Brain Activity in Proceedings of 2012 IEEE-EMBS International Conference on Biomedical and Health Informatics (Jan. 2012), 212–215.

43. Jubran, A. Pulse Oximetry. Critical Care 19, 272. ISSN: 1364-8535 (Dec. 2015).

44. Rwei, A. et al. A Wireless, Skin-Interfaced Biosensor for Cerebral Hemodynamic Monitoring in Pediatric Care. Proceedings of the National Academy of Sciences of the United States of America 117, 31674–31684. ISSN: 0027-8424 (2020).

45. Barkas, D. et al. Sustainable Energy Harvesting through Triboelectric Nano – Generators: A Review of Current Status and Applications. Energy Procedia 157, 999–1010. ISSN: 18766102 (Jan. 2019).

46. Wyser, D. G., Lambercy, O., Scholkmann, F., Wolf, M. & Gassert, R. Wearable and Modular Functional Near-Infrared Spectroscopy Instrument with Multidistance Measurements at Four

Wavelengths. Neurophotonics 4, 041413. ISSN: 2329-423X, 2329-4248 (Aug. 2017).

47. Lacerenza, M. et al. Wearable and Wireless Time-Domain near-Infrared Spectroscopy System for Brain and Muscle Hemodynamic Monitoring. Biomedical Optics Express 11, 5934–5949. ISSN: 2156-7085 (Oct. 2020).

48. Chen, S.-H., Chuang, Y.-C. & Chang, C.-C. Development of a Portable All-Wavelength PPG Sensing Device for Robust Adaptive-Depth Measurement: A Spectrometer Approach with a Hydrostatic Measurement Example. Sensors 20, 6556. ISSN: 1424-8220 (Jan. 2020).

49. Iakovlev, D., Dwyer, V., Hu, S. & Silberschmidt, V. Noncontact Blood Perfusion Mapping in Clinical Applications in SPIE Photonics Europe (eds Popp, J., Tuchin, V. V., Matthews, D. L. & Pavone, F. S.) (Brussels, Belgium, Apr. 2016), 988712.

50. Kim, J. et al. Battery-Free, Stretchable Optoelectronic Systems for Wireless Optical Characterization of the Skin. Science Advances 2, e1600418. ISSN: 2375-2548 (Aug. 2016).

51. Mollerus, F. Literature Survey: The Integration of Diffuse Reflectance Spectroscopy into the Electrosurgical Knife Used during Breast-Conserving Surgery (2018).

52. Callaert, P. Literature Survey: Design of a Smart Electrosurgical Knife for Breast Conserving Surgery (2021).

Appendix

A. Diffuse Reflectance Spectroscopy[1]

Spectroscopy methods such as raman spectroscopy and fluorescence imaging have been gaining traction in clinical practice as they allow for fast and noninvasive tissue discrimination, without altering tissue composition. An exemplary technology is that of diffuse reflectance spectroscopy (DRS), which has been of particular interest in oncology research in the past 20 years due to its capability of differentiating the optical properties of cancerous and healthy tissue. This chapter summarizes the information necessary to understand its working principle, the instrumentation required for this technology and the physical and mathematical assumptions behind it.

A.1. Principles of DRS

A.1.1. Working principle

DRS is a spectroscopic technique which exploits the inherit optical properties of tissue to enable real-time discrimination and quantification of physiological parameters. When light in a large bandwidth of wavelengths is shone through biological tissue, part of it is directly reflected, while a portion penetrates the sample and interacts with the biological molecules inside it. Photons are either scattered or absorbed by the turbid media, leading to a modulation of the light intensity that depends on the optical properties of the specific tissue. The backscattered light is then measured by a spectrometer and a diffuse reflectance spectrum is reconstructed as a function of wavelength. The measured spectral response is associated with chemical and morphological properties of tissue, so that it can be used to extrapolate quantitative physical parameters through mathematical modeling of light propagation and empirical knowledge [51, 52]. The principles of DRS are summarized in A.1.

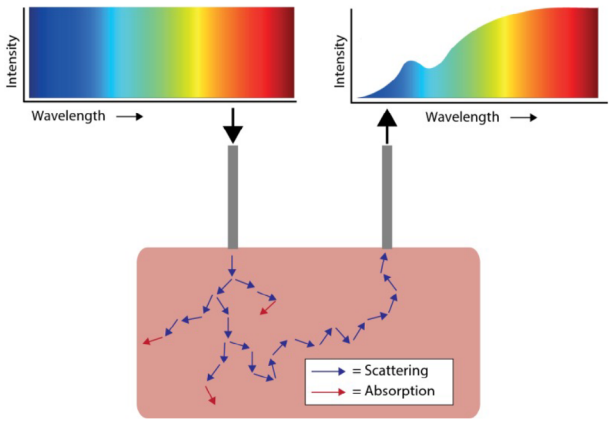

Figure A.1: Schematic representation of DRS principles [34]

A.1.2. Scattering

The path of photons in turbid media is affected by the size, shape, density and refractive index of cellular and subcellular structures. Light scattering happens when the incident direction of a photon changes due to interaction with tissue molecules. It is defined as elastic when the photon's energy isn't affected by this interaction, so that the frequency and wavelength of the scattered radiation are the same as the incident photon. There are two types of elastic scattering, *Rayleigh* and *Mie*, depending on whether the size of the biological structure responsible for the scattering event is smaller or comparable to the photon's wavelength [51].

[1]The principles of DRS were investigated during the literature survey cunducted prior to the thesis project. This appendix corresponds to Ch. 3 of the literature survey report, slightly adapted for this text.

Scattering is qualified by the scattering coefficient μ_s[cm^{-1}], which is dependant on the cellular architecture of the tissue and can be used in DRS to classify it's morphology and structure [28].

A.1.3. Absorption

Absorption of light by cells happens when the wavelength of the incoming photon is in resonance with that of atoms within the cell. In this case the energy of the photon is completely consumed by the atom, which jumps from the current to the excited state without emitting new photons, so that no light is transmitted to other atoms [51]. Chromophores are the particles responsible for light absorption in biological tissue. The main chromophores in soft tissue are β-carotene and hemoglobin, which absorb light in the visible range, and water, lipids and collagen which are dominant at near-infrared (NIR) wavelengths. The absorption capability of each chromophore is related to their concentration according to the *Beer-Lambert law* (described in detail in section A.3), and is quantified by the absorption coefficient μ_a[cm^{-1}]. The absorption spectra of the main tisue chromophores are shown in fig. A.2.

A.1.4. The reflectance spectrum

The absorption and scattering coefficients are wavelength-dependent parameters that represent the probability of a photon to be absorbed or scattered by a certain tissue, and influence the overall reduction in light intensity transmitted through the sample. In DRS, the intensity of the backscattered light is detected as a measure of reflectance, defined as the ratio between light intensity at the receiver and incident light intensity. The diffuse reflectance spectrum measured with a DRS system is then a function of the optical absorption spectrum, defined for each chromophore, and scattering spectrum, dependent on the tissue type [28].

A.2. Instrumentation

A DRS setup is composed of a broadband light source, two optical fibers and spectrometers. Light is transmitted via an optical fiber to the tissue sample, where it interacts with the biological molecules. It is then picked up by the second optical fiber, which transports it to the spectrometer unit. There, light intensity is transformed into a digital signal that is processed to construct the reflectance spectrum.

Light Source

The light source used for DRS is generally a broadband light in the wavelength range of 600-

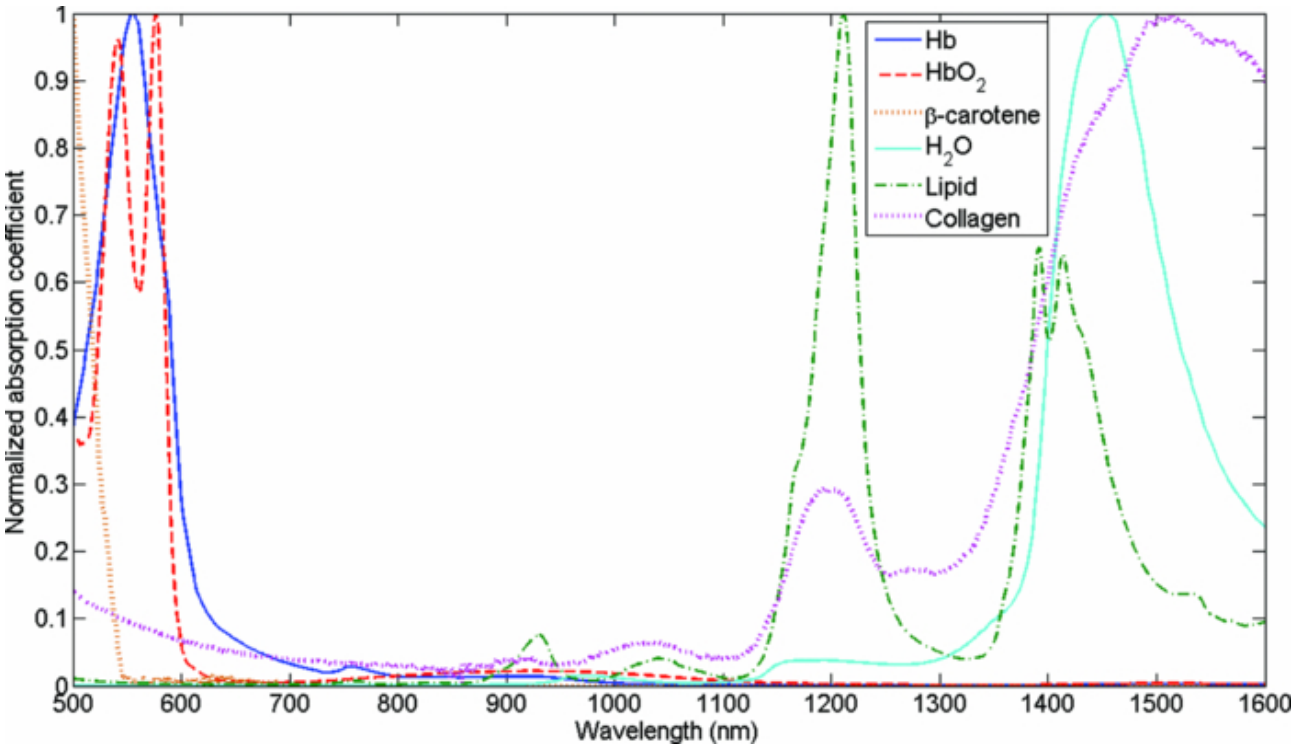

Figure A.2: Normalized absorption spectra of the main tissue chormophores [12]

1100 nm, although studies have shown the benefits of increasing the range until 1600 nm [12, 17]. Careful choice of the spectral range is particularly relevant due to the wavelength-dependency of the tissues optical properties, which also affects the achievable penetration depth, as well as the spectral resolution, of the device [28]. Further considerations concern the power output (or brightness) of the source, which should be high enough to be detectable after interaction with the tissue, while not damaging it. Light sources used in DRS can be pulsed lasers, intensity modulated lasers, and continuous wave sources, which respectively identify time-domain, frequency-domain and steady-state DRS methods [51].

Fiber optic probe

The probe usually consists of two bundles of optical fibers responsible for the transport and collection of light. The optical fiber layout depends on the probe design and influences the probing volume and depth depending on the distance between the source and detector fibers, referred to as source-detector separation (SDS). As the latter increases, so does the sensitivity of the measurement at deeper tissue depth, although this is limited by the light intensity at the receiver to obtain a big enWWvough SNR. Aside from the SDS, the choice of material and number of optical fibers varies depending on the application. Of particular importance is the mounting of the fibers to optimize the probe-tissue interface, which is necessary to limit light interference and measurement errors due to varying pressure and incident angle [51].

Spectrometer

The light collected by the optical fibers passes through a diffraction grating, a dispersing element which divides the light into separate wavelength components. Then, the amount of photons hitting a plate is measured by a single channel detector to record the light intensity at each wavelength and transform it into a digital signal. The spectrometers are then interfaced with computers to acquire the signal and construct the reflectance spectrum in near-real time.

Calibration

Calibration of the DRS unit is necessary to distinguish the effect of ambient light from the sensor's output due to the incident light from the device. For this purpose, a reference recording is first acquired with a sample of known properties (usually a tile of barium sulfate or polytetrafluoroethylene). A background spectrum in absence of the light source can also be recorded and subtracted from the measurements to compensate for external light interference and improve the SNR [51].

A.3. Mathematical modeling of light propagation

In order to extract information regarding chromophore content and other tissue properties from the reflectance spectrum, it is necessary to use mathematical models able to describe light propagation in turbid media (biological tissue). In the context of DRS applications, the most commonly used are the diffusion theory and Monte Carlo simulations.

A.3.1. Diffusion theory

The diffusion theory is an analytical model derived from the radiative transport theory, which describes light propagation in biological tissue. In order to obtain an analytical solution, the diffusion theory introduces a specific set of assumptions [36, 51]:

- Scattering events are isotropic and tissue absorption is small compared to tissue scattering ($\mu_s >> \mu_a$). In order to take into account the anisotropy of biological tissue, the reduced scattering coefficient is used, according to the formula:

$$\mu'_s = \mu_s(1 - g) \qquad \textbf{(A.1)}$$

  Where μ'_s is the scattering coefficient defined as $\mu'_s = a * \lambda^{-b}$, with a and b being tissue-dependent parameters representing the scattering amplitude and slope, respectively. g is the anisotropy factor, which represents the average scattering angle (values of 1 indicate forward, isotropic scattering while values close to 0 are associated with anisotropy).

- The SDS is smaller than inverse of μ'_s, meaning that the source and detector are separated, and light diffuses before reaching the detector.

- The medium is homogeneous and semi-definite, delimited by the probe-tissue interface.

As these assumptions remain valid in the NIR range, this theory is highly valuable in the biomedical field. Under these presumptions, the spatially-resolved diffuse reflectance R can be calculated as a function of μ'_s, μ_a, and the radial distance ρ between the source position z_0 and the detector [51]:

$$R(\rho) = \frac{1}{4\pi}\left[z_0\left(\mu_{eff}+\frac{1}{r_1}\right)\frac{e^{-\mu_{eff}r_1}}{r_1^2} + (z_0+2z_b)\left(\mu_{eff}+\frac{1}{r_2}\right)\frac{e^{-\mu_{eff}r_2}}{r_2^2}\right] \quad \textbf{(A.2)}$$

With $\mu_{eff}=\sqrt{3\mu_a(\mu_a+\mu'_s)}$ being the effective attenuation coefficient, z_b the extrapolated boundary condition and r_1 and r_2 the distances from source and detector, and from source to probed tissue, respectively. From a single reflectance measurement, it is not possible to extract both coefficients values at a certain wavelength, so multiple SDS are required. Alternatively, a priori wavelength-dependent knowledge of scattering and absorption of the chromophores can be used. The total absorption coefficient is described as follows by taking the values of the independent μ_i, i corresponding to each chromophore, from literature.

$$\mu_a(\lambda) = \sum_{i=1}^{N} [c_i] \cdot \mu_{a_i}(\lambda) \quad \textbf{(A.3)}$$

The known values are then used to fit the measured absorption in order to estimate the chromophore concentration $[c_i]$. The total reduced scattering coefficient is evaluated considering the Mie and Rayleigh scattering theories by fitting the non wavelength-dependant parameters [13]:

$$\mu'_s(\lambda) = a_{\text{Mie}}\,\lambda^{-b} + a_{\text{Rayleigh}}\,\lambda^{-4} \quad \textbf{(A.3)}$$

A.3.2. Emprirical models

When probes are miniaturized, the assumption on the SDS is no longer valid, so an analytical solution can't be calculated via the diffusion theory. The same issue holds for when the absorption effect is no longer negligible compared to scattering. In these cases, empirical models can be employed to extract tissue information from reflectance measurements. One approach consists in modeling the reflectance measurements of multiple phantoms with known optical properties, to generate look-up tables. Another in using Monte-Carlo based approaches and linear inversion [35, 36].

All the mentioned approaches have different requirements in terms of necessary computational power and time, prior knowledge and level of approximation. Comprehensive descriptions of their mathematical expression and uses have been presented by F.C.S Mollerus, T. M. Bydlon and R. Nachabé in their thesis reports [35, 36, 51].

A.4. Conclusion

The working principle of DRS was analyzed. The main phenomena affecting light interaction in turbid media, scattering and absorption, are characterized and defined through the scattering and absorption coefficient, which are wavelength-dependent parameters. While scattering depends on tissue morphology and cell structure, absorption is influenced by the different molecules responsible for light absorption in biological media, called chromophores. The reflectance spectrum measured by DRS is then a combination of the contribution of the two parameters and depends on the type of tissue that is probed. The instrumentation required for DRS measurements consists of a broadband light source connected to a fiber optic probe for light transmission; a second probe that collects the backscattered light; and a spectrometer that converts the received light into an intensity signal. From the detected light intensity, a reflectance spectrum is reconstructed according to the diffusion theory. It is then possible to extract the absorption and scattering coefficients and estimate chromophore concentrations through the use of mathematical models, look-up tables and Monte-Carlo simulations. The explained principles lay a base to understand the operation of DRS, necessary to develop a simplified version of this optical spectroscopy technique, which is the aim of the reported thesis project.

B. Circuit Simulation

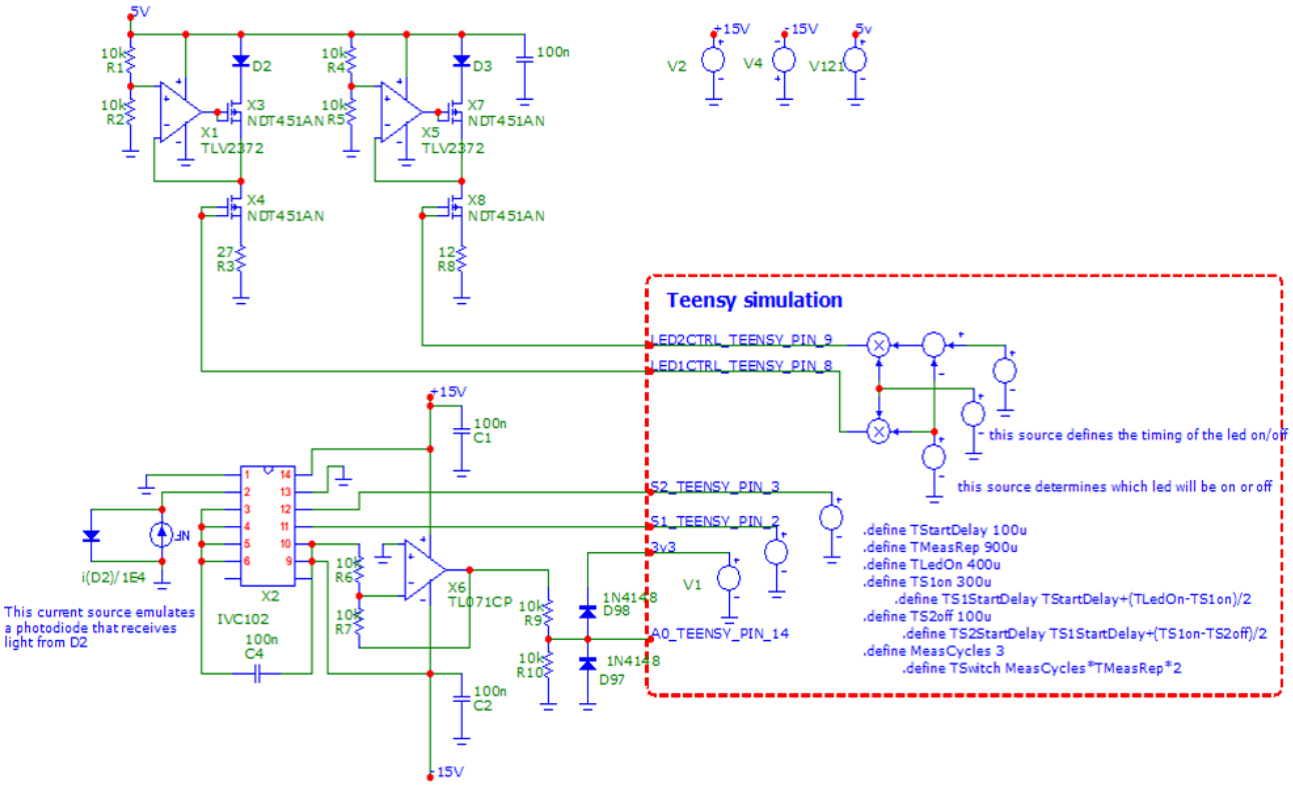

▲

Figure B.1: Schematic used to simulate the behavior of the circuit in MicroCap (Spectrum Software, USA). The simulation was designed by S. Azizian Amiri and F. Budzelaar, and adapted for this project.

C. Phantoms Preparation

Phantom (fat %)	Water	lard	NaCl (1% of water volume)	SB (0.1% of water volume)	Gelatin (15% of water volume)	EL 33 (10% by weight of lard)
0%	100ml	0ml	1g	0.1 g	15 g	-
5%	95ml	5ml	0.95 g	0.095 g	14.25 g	-
10%	90ml	10ml	0.9 g	0.09 g	13.5 g	-
20%	80ml	20ml	0.8 g	0.08 g	12 g	-
30%	70ml	30ml	0.7 g	0.07 g	10.5 g	-
40%	60ml	40ml	0.6 g	0.06 g	9g	-
50%	50ml	50ml	0.5 g	0.05 g	7.5 g	-
60%	40ml	60ml	0.4 g	0.05 g	6g	5.1 g
70%	30ml	70ml	0.3 g	0.04 g	4.5 g	6g
100%	-	100ml	-	-	-	-

▲

Table C.1: Exact quantities of ingredients used for the production of the ten tissue mimicking phantoms, according to the formulas developed by Azizian Amiri et al. and van Berckel [18, 29]. 100 ml of solution were produced for each phantom.

Briefly, to produce the phantoms, water was mixed with salt, baking soda and SB and heated to 50°C on a heater-stirrer. An extra 10 ml of water was added to compensate for evaporation. Gelatin was added to the mixture and heated to 80°C while mixing at 500 rpms. The melted lard (mixed with the emulsifier if necessary) was then added to the water-gelatin mixture at 800 rpms without heat. A cold bath was used to bring the mixture to room temperature. Then, an electronic mixer was used to further emulsify the ingredients. 10 ml of mixture were poured in identical paper cups for each phantom, to obtain discs of about 3 mm thickness. The leftover mixture was poured in another cup for the DRS measurement. The phantoms were then placed in the freezer for one hour, after which they were left in the refrigerator for 12 hours.

D. Scattering Compensation

This appendix is dedicated to developing a possible scattering compensation method. A full study would be required to successfully ideate, test and validate such method. Here, one idea, and the theory behind it, are represented. The method was developed based on prior knowledge and the DRS results, and validated with the LED-test results. The method did not prove successful within the LED-test, and was thus excluded from the report. However, the proposed concept may be useful for future studies, so it is here reported for reference. Recently, Kho et al [30] proposed a method to estimate the f/w-ratio in breast based on the two isosbestic points between the lipid and water absorbance spectra, at 910 nm and 1197 nm, depicted in Fig. D.1.

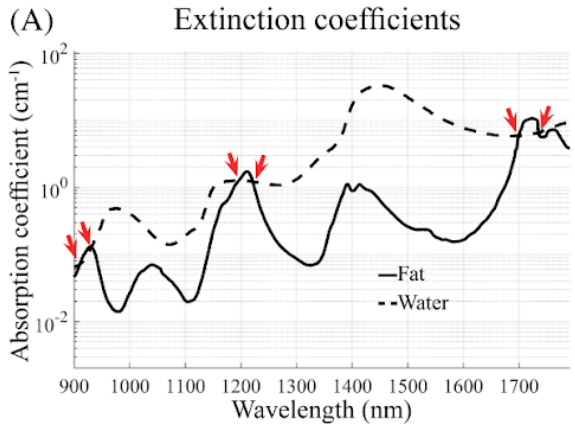

Figure D.1: Absorption coefficients of water and fat, and their isosbestic points. Figure taken from [30].

Their approach hipothesizes that near 1200 nm, since the water and fat have the same absorption, changes in the reflectance spectrum's slope are linearly associated with changes in the tissue composition. In the study, the optimal wavelengths at which slope changes can be observed are at a 10 nm distance from the isosbestic point. Such precision cannot be achieved in the multi-wavelength approach proposed in this thesis project, especially with LEDs. However, the method proposed by Kho et al. served as inspiration to develop a possible scattering compensation method, based on the following idea:

Let us assume that water and fat were the only absorbers in the tissue, and scattering had negligible influence. Theoretically, in these conditions, the isosbestic points indicate that, after scaling at 1200 nm, any reflectance measurement taken at 910 nm should result in the same intensity value. The phantoms used for the tests conducted in this study were mainly composed of fat and water, so it is possible to assume that no other absorbers were present. However, looking at the measured DRS spectra, depicted in Fig. D.2, the intensity at 910 nm varied between phantoms.

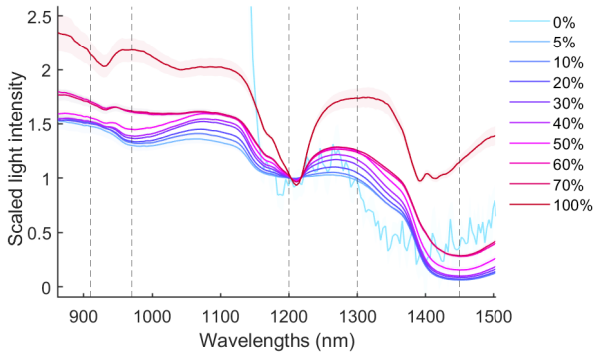

Figure D.2: Mean DRS spectra extracted form the proof-of-concept test measurements, scaled at 1200 nm.

Based on the assumptions, these differences are purely due to scattering. As a result, if the spectra are scaled so that the values at 910 nm correspond, the influence of scattering is eliminated from the measurements. By sampling the scaled reflectance spectra at a wavelength between 910 nm and 1200 nm, the comparison between the resulting values should only contain information regarding

the variations in fat and water contents between phantoms.

The proposed approach was tested on the DRS spectra, as well as the results of the LED-tests, by comparing the intensity values obtained from the first and second set of phantoms, fabricated for the proof-of-concept test (t1) and validation test (t2) respectively. The composition of the phantoms and estimated coefficients are detailed in the respective sections in the report.

To evaluate the validity of the proposed scattering compensation method, the full range reflectance spectra were scaled between 910 nm and 1200 nm. The obtained spectra for both sets of phantoms are depicted in Fig. D.3.

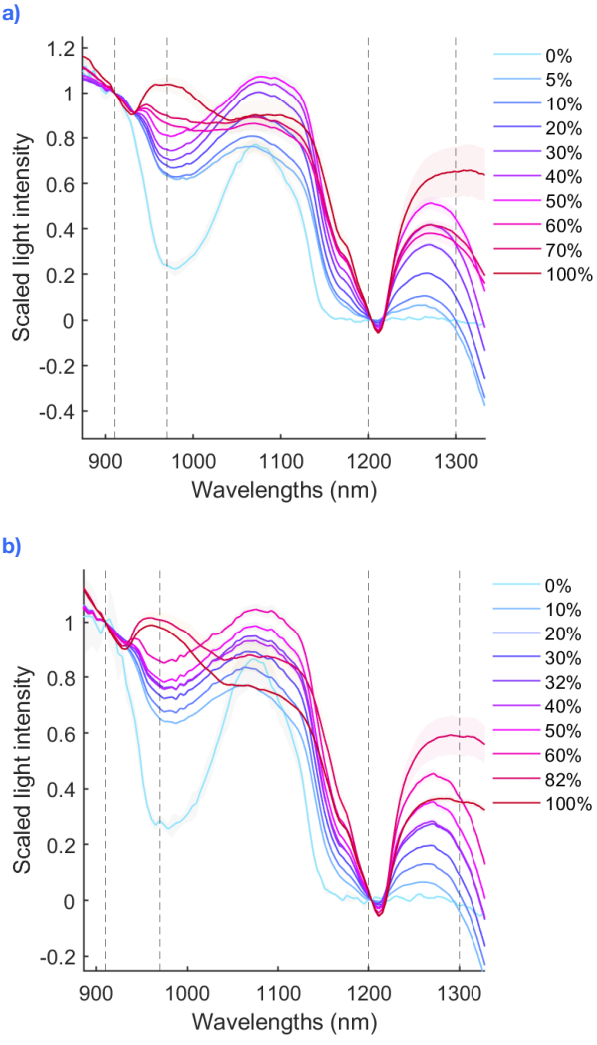

Figure D.3: DRS spectra obtained from the first set of phantoms (a), and the second one (b), scaled at 1200 nm. The dotted lines represent the wavelengths of the LEDs used in the LED-test.

The scaled DRS values at 970 nm were extracted from the graphs, and plotted against the fat percentage to generate the fat-intensity curve. According to the method, the obtained curve should represent a linear relationship between fat and scaled intensity, independent of the scattering properties of the corresponding phantoms. Fig. D.4 shows the curves obtained from the samples DRS spectra of the two phantom sets, in blue and red respectively.

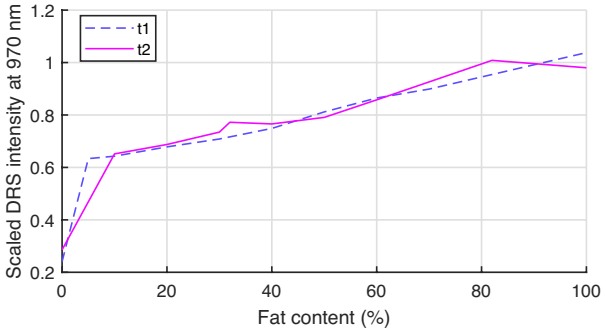

Figure D.4: Fat-intensity curves obtained by sampling the DRS spectra at 970 nm, after scaling between 910 nm and 1200 nm. The blu dashed line was derived from the first phantoms set (t1), while the pink continuous line from the second one (t2).

Here, the two curves are reasonably similar, as expected. The 0% phantom measurements do not follow the linear relationship, but this is explained by the fact that in both cases the 0% sample could not be accurately measured in reflectance configuration due to low scattering and high absorbance of the material. The interesting result is that, although with some deviation, the phantoms associated with a significantly different scattering profile (the 60%, 70% and 100% samples from t1, and the 32%, 82% and 100% samples from t2) still adhere to the linear relationship. From this, we can infer that the influence of scattering is successfully removed, or at least partially reduced.

The same process was replicated with the discrete transmittance spectra constructed from the LED-test measurements. D.5 displays the resulting plots.

Scaling of the discrete spectra measured with the LEDs did not yield the same promising results. Although a gradient can be observed at 1300 nm and 1450 nm in Fig. D.5a, the behavior does not generally follow the same trend as the DRS spectra. A possible explanation may be that, when

looking at the discrete spectra before scaling (not pictured), clear differences were noticeable from the shape of the full-range DRS spectra. Specifically, the values at 910 nm were much lower than expected. As previously mentioned in the test results and discussion, the measured signal was highly subject to variability. As small differences between signals were detected, these variations have a significant impact on the results.

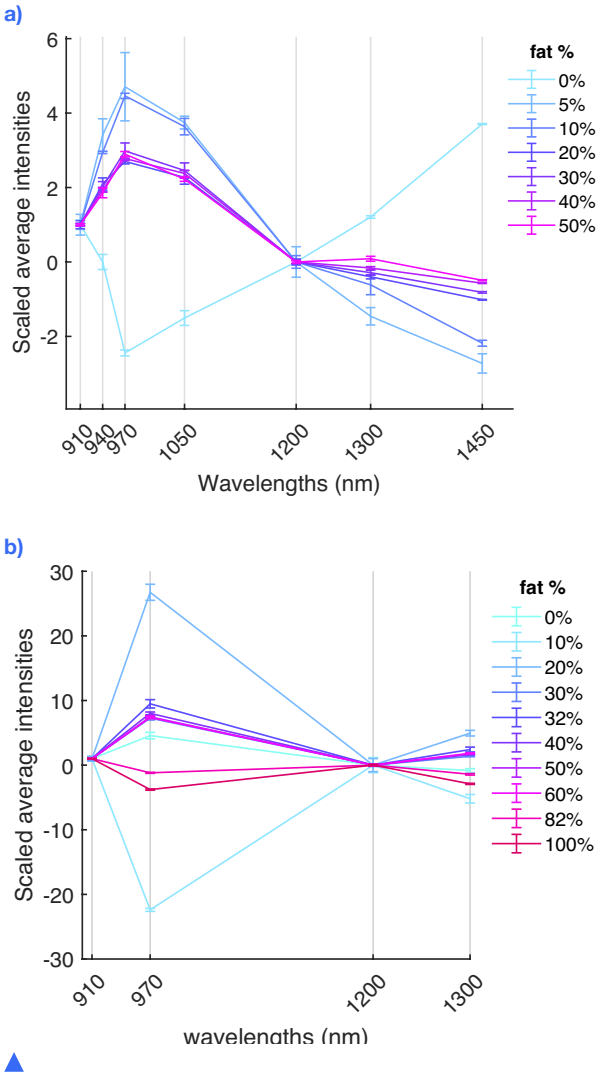

Figure D.5: Discrete transmittance spectra from the two LED-tests, scaled between 910 nm and 1200 nm. (a) Discrete scaled spectra from the proof-of-concept (t1), performed on the first set of phantoms. (b) Discrete scaled spectra from the validation LED-test (t2), performed on the second set of phantoms; only the data from the second day is included for simplicity.

As a result, the LED-results are non conclusive, and seem to invalidate the proposed scattering compensation method. However, this result may be due to limitations of the test setup, rather than inefficacy of the method itself. The promising results of DRS should be investigated further.

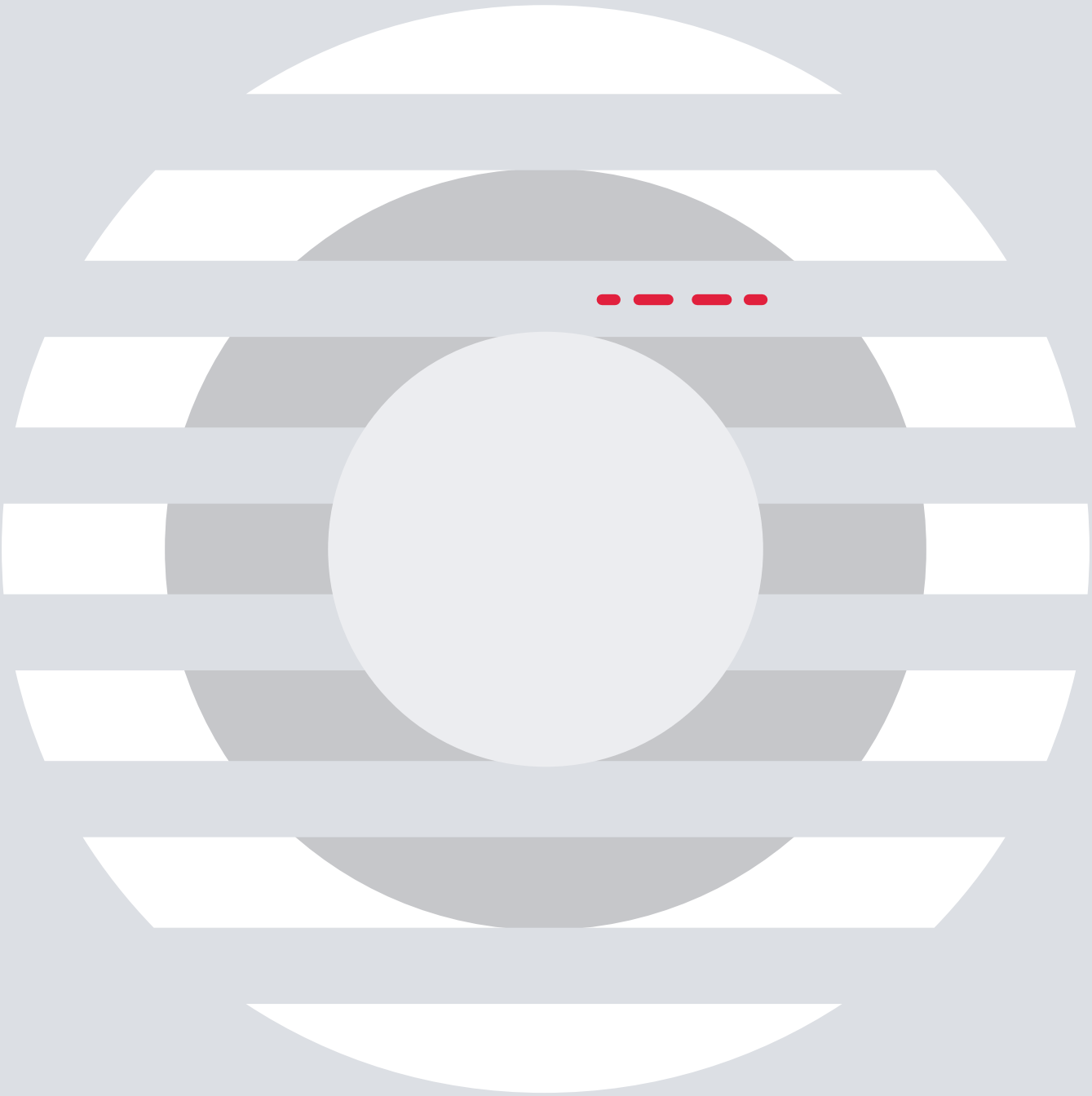

TU Delft